Temporally resolved early BMP-driven transcriptional cascade during human amnion specification

AUTHORS:
Nikola Sekulovski[1], Jenna C. Wettstein[1], Amber E. Carleton[1], Lauren N. Juga[1], Linnea E. Taniguchi[1], Xiaolong Ma[2], Sridhar Rao[1,3,4], Jenna K. Schmidt[5], Thaddeus G. Golos[5,6,7], Chien-Wei Lin[2, †] and Kenichiro Taniguchi[1,3,†]

AFFILIATIONS:
[1]Department of Cell Biology, Neurobiology and Anatomy, Medical College of Wisconsin, Milwaukee, WI 53226, USA
[2]Division of Biostatistics, Institute for Health and Equity, Medical College of Wisconsin, Milwaukee, WI 53226, USA
[3]Department of Pediatrics, Medical College of Wisconsin, Milwaukee, WI 53226, USA
[4]Versiti Blood Research Institute, Milwaukee, WI 53226 USA
[5]Wisconsin National Primate Research Center (WNPRC), Madison, WI, USA
[6]Department of Obstetrics and Gynecology, University of Wisconsin - Madison School of Medicine and Public Health, Madison, WI USA
[7]Department of Comparative Biosciences, University of Wisconsin - Madison School of Veterinary Medicine, Madison, WI, USA

[†]Co-corresponding authors

CONTACT:

Kenichiro Taniguchi
8701 Watertown Plank Road
B4245 BSB CB062
Milwaukee, WI 53226
ktaniguchi@mcw.edu

Chien-Wei Lin
8701 Watertown Plank Road
MEB M1406
Milwaukee, WI 53226
chlin@mcw.edu

ABSTRACT

Amniogenesis, a process critical for continuation of healthy pregnancy, is triggered in a collection of pluripotent epiblast cells as the human embryo implants. Previous studies have established that BMP signaling is a major driver of this lineage specifying process, but the downstream BMP-dependent transcriptional networks that lead to successful amniogenesis remain to be identified. This is, in part, due to the current lack of a robust and reproducible model system that enables mechanistic investigations exclusively into amniogenesis. Here, we developed an improved model of early amnion specification, using a human pluripotent stem cell-based platform in which the activation of BMP signaling is controlled and synchronous. Uniform amniogenesis is seen within 48 hours after BMP activation, and the resulting cells share transcriptomic characteristics with amnion cells of a gastrulating human embryo. Using detailed time-course transcriptomic analyses, we established a previously uncharacterized BMP-dependent amniotic transcriptional cascade, and identified markers that represent five distinct stages of amnion fate specification; the expression of selected markers was validated in early post-implantation macaque embryos. Moreover, a cohort of factors that could potentially control specific stages of amniogenesis was identified, including the transcription factor TFAP2A. Functionally, we determined that, once amniogenesis is triggered by the BMP pathway, TFAP2A controls the progression of amniogenesis. This work presents a temporally resolved transcriptomic resource for several previously uncharacterized amniogenesis states and demonstrates a critical intermediate role for TFAP2A during amnion fate specification.

INTRODUCTION

The amniotic epithelium is the innermost layer of the amniochorionic membrane that physically divides the maternal and fetal environments (Miki et al., 2005; Miki and Strom, 2006). Amniogenesis is initiated during implantation in humans (and in non-human primates), eventually leading to the formation of an amniotic sac structure that surrounds and protects the developing embryo (Enders et al., 1983; Enders et al., 1986; Miki et al., 2005; Sasaki et al., 2016; Shahbazi and Zernicka-Goetz, 2018; Taniguchi et al., 2019). At implantation, the embryo (referred to at this time as a blastocyst) contains three functionally distinct cell types: a collection of unpolarized pluripotent epiblast cells (precursors to the embryo proper and amniotic ectoderm), a surrounding layer of polarized trophectoderm (a placental tissue precursor) and an underlying extraembryonic primitive endoderm (a yolk sac precursor). During implantation, the pluripotent epiblast cells undergo apico-basal polarization to form a cyst with a central lumen, the future amniotic cavity (Carleton et al., 2022). This event is followed by the fate transition of pluripotent epiblast cells at the uterine-proximal pole of the cyst to squamous amniotic ectoderm, forming a sharp boundary between amnion and pluripotent epiblast portions of the cyst (Shahbazi and Zernicka-Goetz, 2018; Shao and Fu, 2022; Taniguchi et al., 2019). This structure, the amniotic sac, represents the substrate for the next essential steps of embryonic development. Recent transcriptomic studies of early human and non-human primate embryos have presented benchmark resources for the amnion transcriptome of primates (Bergmann et al., 2022; Nakamura et al., 2016; Nakamura et al., 2017; Sasaki et al., 2016; Tyser et al., 2021; Yang et al., 2021).

77 The mechanistic dissection of human amnion development presents a challenge,
78 since it is ethically unacceptable to manipulate human embryos *in vivo* and technically
79 difficult to carry out such studies *in vitro*. Non-human primate (NHP) embryos such as
80 rhesus macaque are a suitable alternative to human embryos, due to their close
81 ancestral similarities (Nakamura et al., 2021), and have already provided crucial insights
82 into molecular processes that could potentially regulate amniogenesis. Indeed, genetic
83 manipulation has been demonstrated in NHP systems to study peri-implantation
84 embryogenesis (Yang et al., 2021), although this is not yet a widely applicable approach
85 due to resource availability and logistical complexity of such studies, which also carry
86 their own unique ethical challenges.

87 Previously, we developed an *in vitro* system of human amnion development
88 called Gel-3D (Shao et al., 2017a; Shao et al., 2017b), in which human pluripotent stem
89 cells (hPSC) are plated on a soft gel substrate consisting of extracellular matrix (ECM).
90 Within 24 hours, aggregates of hPSC form polarized cysts composed of columnar
91 pluripotent cells. Over the next three to four days, a 3D environment is introduced by
92 supplementing the culture medium with a diluted ECM overlay. Under these conditions,
93 the initially pluripotent cysts spontaneously undergo squamous morphogenesis, lose
94 pluripotency markers, and begin to express amnion markers; in over 90% of such cysts,
95 the central lumen becomes entirely surrounded by squamous amnion cells (hPSC-
96 amnion, (Shao et al., 2017a)). Using this system, we showed that mechanically
97 activated Bone Morphogenetic Protein (BMP) signaling can trigger amniogenesis and
98 identified several genes that are now used as amnion markers (e.g., GATA3, TFAP2A,
99 GABRP, (Shao et al., 2017a; Shao et al., 2017b)). These findings were supported by

later studies using early human embryo-like models as well as by single cell transcriptomic studies in early human and NHP embryos (Chen et al., 2021; Tyser et al., 2021; Yang et al., 2021; Zheng et al., 2019; Zheng et al., 2022).

Though this Gel-3D system (Shao et al., 2017a) has been valuable in allowing initial investigations of the mechanisms underlying amniogenic differentiation, it suffers from the fact that the initiation of amniogenesis by mechanical cues is stochastic and is not fully penetrant, hindering reproducible examinations into temporally and spatially sensitive processes. To better implement mechanistic studies, we developed a highly reproducible hPSC-based amniogenic system, called Glass-3D^{+BMP}, that does not rely on the mechanically activated spontaneous BMP signaling to initiate amniogenesis. Rather, in Glass-3D^{+BMP}, BMP4 ligand is added exogenously, and the amniotic differentiation response is quickly seen in all cells. Interestingly, while BMP signaling activation is immediately detectable in all cells, squamous morphogenesis (starting approximately 24 hours after BMP4 addition) is initially focal within a given cyst, but then spreads laterally, to form fully squamous amnion cysts by 48 hours. Such amnion cysts (hPSC-amnion) are uniformly composed of mature amniotic cells that share similar transcriptomes with amnion cells from a Carnegie stage (CS) 7 human embryo (dataset from (Tyser et al., 2021)).

Given the robust and synchronous nature of this system, we perform detailed time-course bulk RNA sequencing analyses of developing Glass-3D^{+BMP} hPSC-amnion to comprehensively characterize changes in transcriptional characteristics during the initial stages of amnion fate specification. Strikingly, from 0 to 48 hours after BMP treatment, developing hPSC-amnion displays transcriptomic characteristics of epiblast,

123 intermediate or amnion cells that are present in the CS7 human embryo, revealing a
124 potential amnion differentiation trajectory. Moreover, we systematically characterize
125 dynamically expressed genes, and identify immediate-, early-, intermediate- and late-
126 responding genes associated with amniotic differentiation, some of which are validated
127 and characterized in detail in NHP embryos. Interestingly, in contrast to the previous
128 idea that TFAP2A is a *pan*-amnion marker expressed throughout amniogenesis, we
129 establish that TFAP2A is an early/intermediate responding gene, with a temporal
130 pattern of activation that is distinct from immediate responding genes such as GATA3,
131 another *pan*-amnion marker. Functional analyses show that, in the absence of TFAP2A,
132 amniogenesis is incomplete, suggesting that TFAP2A controls amnion fate progression.
133 Lastly, we identify a population of cells at the boundary of the amnion and the epiblast in
134 the peri-gastrula macaque embryo that shares striking molecular and cellular
135 characteristics of cells undergoing amnion specification in Glass-3D^{+BMP}. Together,
136 using the Glass-3D^{+BMP} amnion platform, these studies present a transcriptomic map of
137 the early stages of amnion differentiation, and identify a critical transcriptional pathway
138 dependent on TFAP2A, as well as a potential site of active amniogenesis in the primate
139 peri-gastrula.
140

141 **RESULTS**

142 **Generation of fully squamous hPSC-derived amniotic cysts in a reproducible and**
143 **controlled manner using a Glass-3D^{+BMP} culture system**

144 Targeted mechanistic investigations into amnion fate specification has been limited by
145 the fact that amniogenesis is not fully penetrant in existing *in vitro* embryo-like models

146 (Chen et al., 2021; Nasr Esfahani et al., 2019; Shao et al., 2017a; Shao et al., 2017b;
147 Zheng et al., 2019), prompting us to explore alternative strategies. Since our previous
148 studies have established that BMP signaling is a major driver of amniogenesis (Shao et
149 al., 2017a; Shao et al., 2017b), we sought to establish a system in which we could
150 directly control the activation of BMP signaling. We began with a culture condition called
151 Glass-3D, in which aggregates of hPSC are cultured in a stiff glass substrate condition
152 with the culture medium supplemented with a 3D ECM overlay (**Fig. 1A**). Under these
153 conditions, aggregates of hPSC initiate radial organization and form cysts with a central
154 lumen within 48 hours (Shao et al., 2017a; Taniguchi et al., 2017; Taniguchi et al.,
155 2015). Importantly, these cysts are composed entirely of polarized pluripotent cells.
156 When we examined the polarized membrane spatial proteomics of these hPSC-
157 pluripotent cysts, we found that BMP receptors are enriched at the basolateral
158 membrane territory (Wang et al., 2021). To test whether BMP signaling could be directly
159 activated in these cysts by the addition of BMP to the medium, pluripotent cysts (derived
160 from H9 (WA09) human embryonic stem cells for all experiments, unless otherwise
161 noted) were treated with exogenously provided BMP4 at d2 (**Fig. 1B**, **Movie 1**, Glass-
162 $3D^{+BMP}$). Nuclear localization of phosphorylated SMAD1/5 (pSMAD1/5), as detected by
163 immunofluorescence (IF), was used as a readout for BMP signaling activation (**Fig. 1C**).
164 At d2 in Glass-3D, prior to the addition of BMP, a polarized pluripotent ($SOX2^{+}$) cyst
165 structure has formed, and a small central lumen is visible (**Fig. 1C** – 0-min); this
166 structure is similar to that of the developing epiblast immediately prior to the initiation of
167 amniogenesis (Shahbazi and Zernicka-Goetz, 2018; Taniguchi et al., 2019). Strikingly,
168 within 10 minutes after BMP addition, uniform nuclear pSMAD1/5 enrichment is seen in

169 all treated cells at an equivalent level (**Fig. 1C** – 10-min, fluorescent quantitation in **Fig.**
170 **1D**). This is quickly followed by the expression of GATA3, a *pan*-amnion marker and a
171 well-known immediate downstream BMP target that has been shown to facilitate
172 pluripotency exit (Gunne-Braden et al., 2020). GATA3 expression is detected in all cells
173 within 3 hours (**Fig. 1E**), suggesting that BMP signaling is uniformly activated.
174 Interestingly, TFAP2A, another transcription factor thought to be an early *pan*-amnion
175 marker, is not detectable in GATA3 positive cells 3 hours after BMP addition (**Fig. 1E**).
176 After 48-hr of BMP4 treatment, all cysts show uniform squamous morphogenesis, loss
177 of pluripotency markers (NANOG, SOX2) and activated expression of additional *pan*-
178 amnion markers, TFAP2A and ISL1 (**Fig. 1F-H**).
179 To investigate whether exogenous BMP4 ligand is continuously needed
180 throughout the 48-hour time-course in order to form fully squamous hPSC-amnion, d2
181 pluripotent cysts were cultured with BMP4 for 24 hours (d2 to d3), then cultured without
182 BMP4 for the following 24 hours (d3 to d4), and then harvested at d4 (4 days after initial
183 plating, **Fig. 1B**). Interestingly, these 24-hr BMP treatment samples show fully
184 squamous amnion cysts that are morphologically and molecularly similar to those
185 treated over 48-hr. That is, they show uniformly squamous cyst morphogenesis and
186 prominent expression of GATA3, TFAP2A and ISL1, (**Fig. 1I,J**, quantitation for
187 fluorescent intensity and nuclear aspect ratios in **Fig. 1K,L**), as well as relatively similar
188 nuclear pSMAD1/5 signals (**Fig. 1M**). Moreover, in the 24-hr BMP treatment samples
189 (**Fig. 2A**), time-course analyses show that heterogeneous GATA3 expression is visible
190 in a few nuclei at 3-hr and 6-hr, becoming more prominent by 12-24-hr (**Fig. 2B-D**).
191 Early GATA3 expression is followed by initiation of TFAP2A expression by 12-hr (**Fig.**

192 **2B,D**). Two other "*pan*-amnion" genes, *ISL1* and *HAND1* become activated by 24-hr
193 (**Fig. 2C,E**), revealing a previously unrecognized GATA3 → TFAP2A → ISL1/HAND1
194 amniotic gene activation order (**Fig. 2B,C**, mRNA expression levels in **Fig. 2D,E**).
195 Importantly, SOX2 expression is abundant at 6-hr, fades in some nuclei at 12-hr and is
196 largely diminished by 24-hr (**Fig. 2B,C**, mRNA expression levels in **Fig. 2F**). NANOG
197 expression follows a similar time course to that of SOX2, revealing a gradual loss of
198 pluripotency (**Fig. 2F**). Samples treated with BMP4 for 24-hr or 48-hr display similar
199 levels of amnion and pluripotency markers (**Fig. 2G**), suggesting that BMP4 treatment
200 may be dispensable after the first 24 hours. To test this possibility, we treated cysts with
201 BMP4 for 24 hours (d2-d3) and subsequently treated with LDN-193189, a small
202 molecule inhibitor for the BMP receptor kinase activity (d3-d4). This treatment resulted
203 in fully squamous cysts that are positive for GATA3 and ISL1/2 (**Fig. 2H**), confirming
204 that BMP signaling initiates the early amniogenesis cascade, but is not required for its
205 progression.
206 Together, these results show that BMP4 treatment of d2 pluripotent cysts in a
207 Glass-3D culture environment provides a robust amniogenic model that enables
208 mechanistic investigations. We confirmed this finding in a human induced pluripotent
209 stem cell line (1196a, **Fig. S1A,B**, (Chen et al., 2014)) as well as in H7 human ESC
210 (**Fig. S1C**), further establishing this protocol as an effective model of amnion fate
211 conversion *in vitro*. Given that BMP4 treatment from d3 to d4 is dispensable, 24-hour
212 BMP4 treatment between d2 and d3 is used in all remaining experiments using Glass-
213 3D^{+BMP}, unless otherwise noted.
214

215 **Transcriptomic characterization of developing Glass-3D^{+BMP} hPSC-amnion**

216 To comprehensively understand the transcriptomic changes during hPSC-amnion
217 development in the Glass-3D^{+BMP} system, we performed bulk RNA sequencing analyses
218 for samples taken at 0-, 0.5-, 1-, 3-, 6-, 12-, 24- and 48-hr timepoints (post-BMP4
219 treatment). Samples were also taken from pluripotent monolayers and d4 pluripotent
220 cysts (**Fig. 3A** (experimental outline), **3B** (heatmap), **3C** (principal component analysis
221 (PCA)), see **Table 1A** for normalized and filtered counts). Overall, a total of 12,891
222 genes were detected among all sequenced samples. Similar to known immediate BMP-
223 responding genes (e.g., *ID2*, *BAMBI*), *GATA3* shows a significant increase by 1-hr, and
224 continuously increases overtime (**Fig. 3D**, >100-fold increase by 1-hr). Other markers
225 also display expected expression patterns (**Fig. 3E-G**). For example, *TFAP2A* and *ISL1*
226 show significant increases by 3-hr and 24-hr, respectively (**Fig. 3E**), and pluripotency
227 markers (**Fig. 3G**, *NANOG*, *OCT4/POU5F1*, *SOX2*) show reduction overtime. A
228 comparison of gene expression between d4 Glass-3D pluripotent cysts and d4 Glass-
229 3D^{+BMP} hPSC-amnion (48-hr timepoint) shows 1,820 upregulated and 2,092 down-
230 regulated (cut-off = 2-fold, $p<0.05$) genes in d4 Glass-3D^{+BMP} hPSC-amnion (**Fig. 3H**,
231 see **Table 1B,C** for full lists). Highly upregulated markers include known advanced
232 amnion state markers such as *GABRP*, *IGFBP3* and *EPAS1* (**Fig. 3H**), and highly
233 downregulated genes include *SOX2* and *NANOG* (**Fig. 3H**, see **Table 1D**,**E** for Gene
234 Ontology (GO) enrichment analyses (Biological Processes) for all significantly
235 upregulated and downregulated genes (> 2-fold, FDR < 0.05)).

236 The transcriptomic characteristics of developing amnion cells from a Carnegie
237 stage (CS) 7 human embryo were recently described by Tyser *et al.* (**Fig. 4A** shows a

238 UMAP (Uniform Manifold Approximation and Projection) plot with the original
239 coordinates and annotations, (Tyser et al., 2021)). In this analysis, the authors state that
240 yolk sac and connecting stalk tissues were discarded during dissection, but amnion
241 tissue was intact and included in the single cell preparation that was analyzed (Tyser et
242 al., 2021). Consistent with this notion, our analysis in which expression was
243 superimposed on the UMAP plot shows that *pan*-amnion markers such as *GATA3*,
244 *TFAP2A* and *ISL1* are broadly expressed in the rod-shaped cell population marked
245 "Ectoderm" (**Fig. 4B**, areas within the inset "**i**" are shown in **4B-D**; see **Fig. S2A** for
246 uncropped UMAP expression plots), suggesting that this region contains cells of the
247 amniotic lineage. We next examined which cells in the CS7 human embryo share
248 transcriptomic similarities to developing hPSC-amnion, and found that, indeed, the 48-hr
249 Glass-3D^{+BMP} samples exhibit clear transcriptional similarities to cells marked
250 "Ectoderm" in the CS7 human embryo (**Fig. 4C**), validating the human amnion-like
251 characteristics of our hPSC-amnion model. Interestingly, the earlier timepoints also
252 show overlaps with cell types of the CS7 human embryo (**Fig. 4C**, uncropped plot
253 shown in **Fig. S2B**). While pluripotent monolayer, d4 Glass-3D pluripotent cyst, as well
254 as 0-, 0.5-, 1-, 3- and 6-hr samples transcriptomically resemble Tyser "Epiblast" cells
255 (orange dots in **Fig. 4C**), 12-hr samples show transcriptomic similarities with cells
256 labeled in the Tyser analysis as "Primitive Streak"; these cells map close to the
257 Epiblast/Primitive Streak boundary in the Tyser UMAP (green dots in **Fig. 4C**). By 24-hr,
258 the transcriptomes are most similar to Tyser "Primitive Streak" cells proximal to the
259 amniotic "Ectoderm" (blue dots in **Fig. 4C**). Despite their "Primitive Streak" annotation,
260 these 24-hr cells adjacent to the amniotic "Ectoderm" population display relatively low

261 levels of *TBXT* (a major marker of primitive streak cells, **Fig. 4D**, (Beddington and
262 Robertson, 1999; Tyser et al., 2021; Zheng et al., 2019)), marking them as distinct from
263 the *TBXT*^{high} "Primitive Streak" cells progressing to "Nascent Mesoderm" (**Fig. 4D**).
264 Indeed, in developing hPSC-amnion, while not detectable using IF (**Fig. S2C**), a
265 *TBXT*^{low} transcriptional state is seen starting at the 24-hr timepoint (**Fig. S2D**). A similar
266 trajectory as well as gene expression patterns are also seen in the Yang *et al.* (Yang et
267 al., 2021) cynomolgus macaque peri-gastrula single cell RNA sequencing dataset (**Fig.
268 4E-G,** uncropped plots shown in **Fig. S2E,F**). These bioinformatic analyses suggest that
269 the Glass-3D^{+BMP} amnion may develop from pluripotent epiblast-like cells that are
270 transcriptomically equivalent to the CS7 epiblast cells, and, then traverse *TBXT*^{low}
271 intermediate states as the lineage specification continues before acquiring an amniotic
272 fate by 48-hr (dotted arrow, **Fig. 4C**).
273 Given that the hPSC-amnion differentiation trajectory in the Glass-3D^{+BMP} model
274 overlaps with cells in the CS7 human embryo, it appears that active amniogenesis
275 processes may be present in the early post-implantation embryo. Thus, we applied an
276 RNA velocity analysis (Bergen et al., 2020) to the Tyser data; in such an analysis,
277 lineage progression is inferred from comparing spliced and unspliced mRNA. **Fig. 5A**
278 (inset "**i**") shows that the Tyser velocity data show differentiation trajectories very similar
279 to the one inferred from the time-course analysis of the Glass-3D^{+BMP} model.
280 To further validate this notion in a non-human primate system, we performed
281 detailed IF expression analyses for GATA3, TFAP2A, ISL1 and SOX2 in an early
282 cynomolgus macaque embryo staged between CS6 and CS7 (**Fig. 5B-E**). In this CS6/7
283 embryo, a clear amniotic sac is seen, with SOX2^{+} epiblast cells on one side and

284 contiguous ISL1$^+$ squamous amniotic ectoderm cells that are also positive for GATA3
285 and TFAP2A on the other (**Fig. 5B-E**, fluorescent intensity quantitation shown in **5C,E**).
286 Surface ectoderm bridging neural ectoderm and amniotic ectoderm is not seen at this
287 stage; this finding is consistent with the previous histological studies in human (the
288 Carnegie Collection, found in the Virtual Human Embryo Project) and NHP pre- and
289 peri-gastrula embryos (Enders et al., 1983; Enders et al., 1986; Yang et al., 2021).
290 Although amniotic mesenchyme is not evident, some mesenchymal cells are observed
291 underlying the epiblast (**Fig. 5F**, green dotted bracket). These mesenchymal cells show
292 abundant nuclear pSMAD1/5 (**Fig. 5F**) and TBXT (**Fig. S2G**); these cells are likely
293 derived from the primitive streak. Strikingly, at the boundary between the epiblast and
294 amnion, a gradual transition in cell morphology is readily seen: while cells most proximal
295 to the epiblast are columnar, there is a gradual reduction in height until fully squamous
296 cells are seen (**Fig. 5B,D,F,H**), represented by the changes in nuclear aspect ratio (**Fig.
297 5H**). Molecularly, the expression of GATA3, TFAP2A, ISL1 and SOX2 is correlated with
298 such columnar to squamous cell shape change (**Fig. 5B-E**). While SOX2 expression
299 shows a reducing trend, the expression of GATA3, TFAP2A and ISL1 gradually
300 increases in more distal squamous cells (**Fig. 5B-E**, quantitation in **5C,E**). Furthermore,
301 GATA3, TFAP2A and ISL1 each display distinct expression patterns within the
302 boundary cell population, as the expression of GATA3 and TFAP2A is first detected in
303 columnar SOX2$^+$ cells, but in these cells, ISL1 is not observed (**Fig. 5C**). However, a
304 weak but clear expression of ISL1 can be found within ~10 distally located cells, from
305 the first detected GATA3$^+$/TFAP2A$^+$ cell. Similar observations are seen in another early
306 cynomolgus macaque embryo (**Fig. S3**, staged at CS7). This cell shape change

307 associated with the ordered transcriptional events (from GATA3, TFAP2A then ISL1) is
308 similar to the ordered morphological and molecular changes seen in developing Glass-
309 3D^{+BMP} hPSC-amnion. Thus, the results based on these bioinformatic and expression
310 analyses provide evidence for the presence of amniotic fate progression in early post-
311 gastrula embryos at the boundary between amnion and epiblast (a schematic model
312 shown in **Fig. 5I**).
313

314 **Gene expression dynamics in developing Glass-3D^{+BMP} hPSC-amnion**

315 To identify key players potentially involved in amnion fate specification at different
316 stages, we comprehensively characterized all significantly upregulated genes based on
317 when significant upregulations are seen: "immediate" (**Table 2A**, up in 0.5- or 1-hr
318 samples), "early" (**Table 2B**, 3- or 6-hr), "intermediate-1" (**Table 2C**, 12-hr),
319 "intermediate-2" (**Table 2D**, 24-hr) and "late" (**Table 2E**, 48-hr); genes that were kept
320 after a more stringent filtering (described in Materials and Methods) are shown in **Fig.**
321 **6**), enabling the identification of additional temporal markers.

322 Previous studies have identified several *pan*-amnion markers that are known
323 immediate BMP targets (e.g., *GATA3* and others in the list of "immediate" genes, **Table**
324 **2A**), which are expressed in other early BMP-driven tissue morphogenesis. Among the
325 known *pan*-amnion markers, ISL1 is a highly promising marker for early lineage
326 specified amnion cells (Yang et al., 2021; Zhao et al., 2021; Zheng et al., 2022). In
327 accord with this, we found that ISL1 expression is limited to squamous amnion cells and
328 is not seen in the epiblast or in transitioning boundary cells (**Fig. 5B**). Notably, in Glass-
329 3D^{+BMP}, *ISL1* first shows a significant upregulation at 24-hr (intermediate -2, **Fig. 7A**).

330 This correlates with the timeframe at which squamous cells are first observed (**Fig. 2**).
331 This finding suggests that amnion specification is likely initiated prior to 24 hours in
332 Glass-3D^{+BMP} and that genes that are upregulated between 12-24-hr could be used as
333 additional markers for amnion specification. Consistent with the studies by Tyser *et al.*,
334 we identified *DLX5* (716.76-fold increase between 12- and 24-hr, and 2.4-fold increase
335 from 24- to 48-hr, **Fig. 7B**). Interestingly, however, our expression analysis of the Tyser
336 *et al.* dataset reveals a broader *DLX5* expression pattern compared to *ISL1* (the *DLX5*
337 expression domain map is similar to that of *TFAP2A*, **Fig. 4B**). Indeed, our IF analyses
338 for DLX5 in developing hPSC-amnion as well as in a CS7 cynomolgus macaque
339 embryo show expression patterns similar to TFAP2A (**Fig. 7C,D**). These results further
340 validate ISL1 as a marker for specified amnion cells and establish that DLX5 as an
341 additional marker for cells undergoing amniogenesis as well as mature amnion cells.
342

343 **Functional tests of an immediate-, GATA3, and an early-, TFAP2A, responding**
344 **transcription factors**

345 Immediate- and early-responding transcription factors are functionally relevant
346 candidates that initiate amnion specification and drive the expression of early amnion
347 lineage specified markers such as ISL1. Among the genes in the immediate- and early-
348 responding categories, we screened for genes associated with transcription, and
349 identified several genes, including immediate – GATA3 and early – TFAP2A. As noted
350 above, GATA3 expression precedes TFAP2A expression by approximately 9 hours.
351 Both of these factors show highly enriched expression, and both have previously
352 established functions as pioneer transcription factors (Rothstein and Simoes-Costa,

353 2020; Takaku et al., 2016; Tanaka et al., 2020; Van Otterloo et al., 2022; Zaret and
354 Carroll, 2011). Therefore, we examined the role of GATA3 and TFAP2A by generating
355 hPSC-amnion in Glass-3D^{+BMP} derived from H9 cells lacking GATA3 or TFAP2A (two
356 clonal lines with unique mutations were used for each analysis, see **Fig. S4** for KO
357 validation). Interestingly, *GATA3*-KO hPSC grown in Glass-3D^{+BMP} develop into fully
358 squamous cysts that express amnion markers, perhaps suggesting functional
359 redundancy. In contrast, while controls show uniformly squamous amniotic cells at 48-
360 hr, *TFAP2A*-KO cysts contain both squamous (ISL1^{+}) and columnar (NANOG^{+}/SOX2^{+})
361 cell populations (**Fig. 8A** (Glass-3D hPSC-pluripotent cysts),**8B,C** (Glass-3D^{+BMP} hPSC-
362 amnion cysts)). Indeed, a doxycycline inducible expression of TFAP2A in the KO
363 background leads to control-like squamous morphogenesis as well as uniform
364 expression of GATA3 and ISL1 by 48-hr (d4, **Fig. 8C**). These results suggest that
365 amniogenesis may be halted in the absence of *TFAP2A*. To examine this further at
366 transcriptomic levels, we performed time-course bulk RNA-seq for control and *TFAP2A*-
367 KO hPSC-amnion at 0-, 12-, 24- and 48-hr, and performed a transcriptome similarity
368 analysis using the Tyser *et al.* human CS7 embryo dataset. Indeed, while an expected
369 Epiblast to Ectoderm differentiation trajectory similar to **Fig. 4C** is found in controls (**Fig.
370 8D**, left), *TFAP2A*-KO samples do not overlap with Ectoderm cells, even at 48-hr (**Fig.
371 8D**, right). Rather, 48-hr *TFAP2A*-KO samples show transcriptomic characteristics
372 similar to some Primitive Streak cells (**Fig. 8D**, uncropped plots shown in **Fig. S5**), and,
373 strikingly, our IF analysis shows that some cells robustly expressing TBXT^{+} are seen in
374 *TFAP2A*-KO cysts at 48-hr (**Fig. 8E**). These results reveal a paused amniogenesis

375 phenotype in the absence of TFAP2A, providing a previously unrecognized notion that
376 TFAP2A is critical for maintaining amnion fate progression.
377
378 **DISCUSSION**
379 In this study, we developed a reproducible and faithful model for robust mechanistic
380 examinations of human amnion fate specification, and identified a BMP4-dependent
381 amniogenic transcriptional cascade, as well as a role for TFAP2A in maintaining amnion
382 fate progression. Moreover, we established DLX5 as an additional marker for lineage
383 progressing amnion cells and provided evidence for an active amniogenic
384 transcriptional cascade at the epiblast/amnion boundary in peri-gastrula human and
385 non-human primate embryos. These findings and the temporally resolved amniogenic
386 gene lists provided in this study offer additional avenues for further exploration of
387 human amniogenesis.
388 Previous studies established several broad amnion markers (e.g., GATA3,
389 TFAP2A and ISL1) that are expressed in developing, as well as, differentiated amnion
390 cells. However, comprehensive studies have not been performed to fully characterize
391 how each of these markers corresponds to amnion fate specification steps, especially
392 since BMP signaling is a primary trigger of amniogenesis and a large set of BMP target
393 genes are activated. In this study, a time-course transcriptomic analysis was employed
394 to identify genes that display temporal-specific dynamics among genes that show more
395 static expression patterns: this enabled us to define “stage specific” genes that can be
396 used to distinguish amniogenic fate progression states. In particular, we found that
397 *GATA3* is an immediate BMP target during amniogenesis (along with other known

398 targets such as *ID1*, *ID2* and *BAMBI*); a similar BMP4 → GATA3 transcriptional pathway
399 has been well-established previously in other systems (Abe et al., 2021; Bonilla-Claudio
400 et al., 2012; Gunne-Braden et al., 2020; Vincentz et al., 2016).

401 Early activation of GATA3 is followed by the expression of second-tier "early"
402 genes such as *TFAP2A* by 6-hr (clear TFAP2A protein is detected by 12-hr). Our
403 functional analyses indicate that loss of TFAP2A results in incomplete amniogenesis,
404 with failure to downregulate pluripotent genes, loss of some differentiated amnion
405 markers, and, in some cells, increased expression of TBXT, a primitive streak marker.
406 Thus, TFAP2A, a previously recognized pioneer factor (Rothstein and Simoes-Costa,
407 2020; Van Otterloo et al., 2022), appears to be an important component that ensures
408 the proper progression of the amniogenesis process, perhaps by suppressing the
409 TBXT^{high} primitive streak-like state.

410 Interestingly, a recent study by Castillo-Venzor *et al.* reported that, in contrast to
411 our findings, amniogenesis appears intact in the absence of *TFAP2A* (Castillo-Venzor et
412 al., 2023). However, there are multiple differences between the system utilized by
413 Castillo-Venzor *et al. vs.* the one reported here. Castillo-Venzor *et al.* employ an hPSC-
414 based primordial germ cell-like cell (PGCLC) differentiation culture protocol, in which
415 amniotic and mesodermal cells are also formed. In that system, embryoid bodies are
416 generated from hPSC treated with Activin A and CHIR (a small molecule WNT activator)
417 to form "pre-mesodermal cells", and then are grown in the presence of exogenous BMP,
418 SCF (stem cell factor, encoded by *KITLG*), EGF (epidermal growth factor) and LIF
419 (leukemia inhibitory factor) as floating aggregates. Moreover, while uniform
420 amniogenesis is seen in Glass-3D^{+BMP} (a characteristic that enables robust mechanistic

421 examinations specifically into amnion fate progression), the PGCLC differentiation
422 culture used by Castillo-Venzor *et al.* leads to the formation of cells of multiple lineages.
423 Therefore, the loss of TFAP2A in that system may be compensated by signaling factors
424 provided by mesodermal and/or PGCLC. Alternatively or additionally, it is possible that,
425 in this PGCLC culture, while initial amniogenesis might be present (similar to the focal
426 amniogenesis seen in our system), the later fate spreading event may be absent,
427 perhaps due to differences in tissue geometry (aggregates versus cysts), or due to
428 differences in degrees of lineage commitment by the time that spreading can occur.
429 Together, these results suggest that a single lineage culture system (lacking additional
430 cell types), such as the one we describe here, may more readily expose certain critical
431 events and, therefore, in some cases, may more robustly enable mechanistic
432 investigations into lineage progression.

433 Several hours following the activation of *TFAP2A*, third-tier "intermediate" genes
434 such as *ISL1* (ISL1 protein by 24-hr: only in squamous cells) are expressed. It has been
435 previously established that *ISL1* is a key amnion marker in early primate embryos (Yang
436 et al., 2021; Zhao et al., 2021; Zheng et al., 2022). Interestingly, our IF analyses of early
437 peri-gastrulation cynomolgus macaque embryos show that ISL1 expression is restricted
438 to amnion cells that are already squamous in nature (**Fig. 5**). Additionally, our time-
439 course transcriptomic analyses in Glass-3D^{+BMP} reveal that *ISL1* expression is seen at
440 12-24-hr, later than *TFAP2A* activation but much earlier than activation of more
441 differentiated amnion markers such as *GABRP*, *EPAS1* and *IGFBP3* (48-hr). Together,
442 these results suggest that amnion cells progress from GATA3^{+}, to GATA3^{+}/TFAP2A^{+}, to

443 GATA3^{+}/TFAP2A^{+}/ISL1^{+}, to mature amnion cells that express these three markers as
444 well as the more mature amnion markers such as GABRP, EPAS1 and IGFBP3.
445 The first amniogenesis event is seen upon implantation, in the epiblast cells
446 underlying the polar trophectoderm, establishing the amniotic sac, an asymmetric
447 amnion-epiblast cystic structure (Enders et al., 1983; Enders et al., 1986; Shahbazi and
448 Zernicka-Goetz, 2018; Taniguchi et al., 2017). In this study, we provide evidence for the
449 active progression of amniogenic fate conversion at the amnion-epiblast boundary of
450 the cynomolgus macaque peri-gastrula. What is the difference between amniogenesis
451 that occurs during implantation and during gastrulation? A previous study by Sasaki *et*
452 *al.* (Sasaki et al., 2016) showed that, in a macaque embryo staged at PreG1 (just
453 initiating implantation), a stage before *BMP4* expression is seen in the amnion at
454 PreG2, *BMP2* is abundantly expressed in the visceral endoderm. However, the visceral
455 endoderm underlies the epiblast population that gives rise to the embryo proper (not
456 amnion), and *CER1* is also abundantly expressed in the visceral endoderm (Sasaki et
457 al., 2016). Thus, BMP2 in the visceral endoderm in PreG1 embryo is thought not to be
458 the trigger for the initial amniogenesis processes that forms the amniotic sac, and it is
459 currently unclear how BMP signaling is activated in the nascent amnion cells during
460 implantation *in vivo*. Using a Gel-3D hPSC-amnion system, we previously showed that
461 amniogenesis is mechanosensitive, and that a soft substrate can induce BMP signaling
462 in a mechanically dependent manner in developing hPSC aggregates/cysts. This
463 suggests that mechanical signaling might play an important role in the initial BMP
464 signaling activation and downstream amniogenesis during implantation *in vivo*. In
465 contrast, since a continuous BMP signaling cascade is established in epiblast cells of

466 the early primate gastrula (e.g., driving primitive streak formation, primordial germ cell
467 formation), we speculate that the amniogenesis process that occurs during and post
468 gastrulation may be independent of a mechanical cue. It is, however, important to note
469 that the pluripotency states are distinct in the epiblast cells during implantation
470 compared to during gastrulation; it has been suggested that the epiblast cells are in the
471 formative state during implantation and in the primed state during gastrulation (Kinoshita
472 and Smith, 2018; Shahbazi et al., 2017; Smith, 2017). Thus, it is possible that the
473 mechanisms regulating responses to BMP ligands, as well as BMP-dependent
474 transcriptional machineries may differ.

475 Overall, our detailed temporally resolved analyses of Glass-3D^{+BMP} hPSC-
476 amnion development, combined with validation in early macaque embryos has revealed
477 several previously unrecognized findings with implications for BMP-dependent
478 amniogenic transcriptional machineries during amniogenesis, mechanisms continuing
479 amniogenesis in peri-gastrula macaque embryos, and functional characterization of the
480 transcriptional machinery required for amnion fate specification.

481

482 **MATERIALS AND METHODS**

483 *hESC lines*

484 Two human embryonic stem cell lines, H9 (WA09, P30, P48, WiCell; NIH registration
485 number: 0062) and H7 (WA07, P50, WiCell; NIH registration number: 0061), were used
486 in this study. All protocols for the use of hPSC lines were approved by the Human Stem
487 Cell Research Oversight Committee at the Medical College of Wisconsin. All hPSC lines
488 were maintained in a feeder-free system for at least 20 passages and authenticated as

489 karyotypically normal at the indicated passage number. Karyotype analysis was
490 performed at Cell Line Genetics. All hPSC lines tested negative for mycoplasma
491 contamination (LookOut Mycoplasma PCR Detection Kit, Sigma-Aldrich). All transgenic
492 and KO hESC lines in this study used H9 as the parental line. In summary, hESC were
493 maintained in a feeder-free culture system with mTeSR1 medium, or with 50%/50% mix
494 of mTeSR1 and mTeSR plus (STEMCELL Technologies). hESC were cultured on 1%
495 (v/v) Geltrex (Thermo Fisher Scientific), or with Cultrex SCQ (Bio-techne) coated 6 well
496 plates (Nunc). Cells were passaged as small clumps every 4 to 5 days with Dispase
497 (Gibco). All cells were cultured at 37°C with 5% CO_2. Media was changed every day.
498 hESC were visually checked every day to ensure the absence of spontaneously
499 differentiated, mesenchymal-like cells in the culture. Minor differentiated cells were
500 scratched off the plate under a dissecting scope once identified. The quality of all hESC
501 lines was periodically examined by immunostaining for pluripotency markers and
502 successful differentiation to three germ layer cells.
503
504 *Cynomolgus macaque*
505 *Animals*
506 The female and male cynomolgus macaque were housed and cared for at the Wisconsin
507 National Primate Research Center (WNPRC). All procedures were performed in
508 accordance with the NIH Guide for the Care and Use of Laboratory Animals and under
509 approval of the University of Wisconsin College of Letters and Sciences and Vice
510 Chancellor Office for Research and Graduate Education Institutional Animal Care and
511 Use Committee (protocol g005061).

512

513 *Animal breeding and pregnancy detection*

514 Beginning on day 8 post-onset of menses, the female was housed with a compatible
515 male and monitored for breeding. Animals were pair-housed until day 16-20 post-onset
516 of menses. A 2-3 mL blood draw was performed daily from day 8 post-onset of menses
517 until day 16 to assess the timing of ovulation based on the estradiol peak and rise in
518 progesterone in serum. Serum samples were analyzed for estradiol (25 μL) and
519 progesterone (20 μL) using a cobas e411 analyzer equipped with
520 ElectroChemiLuminescence technology (Roche, Basal, Switzerland) according to
521 manufacturer instructions. Results were determined via a calibration curve which was
522 instrument-generated by 2-point calibration using traceable standards and a master
523 curve provided via the reagent barcode. Inter-assay coefficient of variation (CV) was
524 determined by assaying aliquots of a pool of rhesus plasma. For estradiol, the limit of
525 quantitation (LOQ) was 25 pg/mL, the intra-assay CV was 2.02%, and the inter-assay
526 CV was 5.05%. For progesterone, the LOQ was 0.2 ng/mL, the intra-assay CV was
527 1.37%, and the inter-assay CV was 4.63%. A transabdominal ultrasound was performed
528 to detect pregnancy as early as 14 days post-ovulation. The ultrasound measurements
529 in combination with the timing of ovulation were used to estimate the day of conception
530 and gestational age of the pregnancy.

531

532 *Terminal perfusion uterine collection, paraffin embedding, sectioning and staining*

533 The pregnant female was sedated with intramuscular ketamine (>15 mg/kg) followed by
534 IV sodium pentobarbital (>35 mg/kg) and then perfused with 4% paraformaldehyde (PFA)

535 via the left ventricle. The entire uterus and cervix were removed. The serosa and
536 superficial myometrium were scored for better fixative penetration and to denote dorsal
537 and ventral orientation. Tissues were fixed in 4% PFA with constant stirring and solution
538 changes were performed every 24 hours for a total of 72 h. The uterus was serially
539 sectioned from the fundus to the internal cervical os into 4 mm slices using a dissection
540 box. Cassettes with tissue sections were transferred into 70% ethanol, routinely
541 processed in an automated tissue processor and embedded in paraffin for histological
542 analyses (5 μm sections). Fixed uterine tissue were cut in 5 μm thick cross-sections,
543 mounted on slides, deparaffinized in xylene and rehydrated in an ethanol series. Antigen
544 retrieval was performed by boiling in citrate buffer. Sections were blocked 4% goat serum
545 in PBS at RT for at least 3-hr. Subsequent immunolocalization was performed using
546 commercially available primary antibodies, incubated overnight at 4 °C in 4% serum, at
547 the dilutions as shown in **Table 3**. Immunofluorescent detection was performed using
548 secondary antibodies tagged with a fluorescent dye (fluorophores excitation = 488, 555,
549 and 647nm), and counterstained with DAPI. Negative controls were performed in which
550 the primary antibody was substituted with the same concentration of normal IgG of the
551 appropriate isotype. Images were obtained with a Zeiss LSM980 microscope.
552
553 *Glass-3D^{+BMP} hPSC-amnion formation assays*
554 Glass-3D protocol used to generate hPSC-pluripotent cysts was previously described
555 (Hamed et al., 2023; Shao et al., 2017a; Taniguchi et al., 2017; Taniguchi et al., 2015).
556 In brief, hPSC monolayers were dissociated using Accutase (Sigma-Aldrich) at 37 °C for
557 10 min, centrifuged and resuspended in mTeSR1/mTeSR plus 50:50 mix containing 10

558 μM Y-27632 (STEMCELL Technologies). hPSC were plated as single cells at 20,000
559 cells cm^{-2}, unless otherwise specified, onto a 1% (v/v) gel coated wells (Geltrex
560 (Thermo Fisher Scientific), or with Cultrex SCQ (Bio-techne)). After 24 hours (on day 1),
561 culture medium was replenished with fresh mTeSR1/mTeSR plus 50:50 media without
562 Y-27632, supplemented with 2% (v/v) Geltrex or with Cultrex SCQ. Thereafter, media
563 change was performed daily until day 4 (using mTeSR1/mTeSR plus 50:50 media
564 supplemented with 1% (v/v) Geltrex or with Cultrex SCQ), unless otherwise noted. This
565 Glass-3D culture condition results in the formation of hPSC-cysts, cysts with a central
566 lumen surrounded by pluripotent columnar cells. The Glass-$3D^{+BMP}$ culture condition
567 was used to generate hPSC-amnion, cysts with a central lumen surrounded by
568 squamous amnion-like cells. To induce amniogenesis, exogenous BMP ligand
569 (20ng/mL, Bio-techne) was added to developing pluripotent cysts between day 2 to 3 for
570 24 hours, or between day 2 to 4 for 48 hours, unless otherwise noted (e.g., for time-
571 course analyses). Samples were harvested at day 4 (48-hr since starting BMP4
572 treatment). LDN-193189 (500nM, STEMCELL Technologies) was used to disrupt BMP
573 signaling.
574
575 *DNA constructs*
576 *piggyBac-CRISPR/Cas9 (pBACON) constructs*
577 A piggyBac-CRISPR/Cas9 (pBACON) vector that contains SpCas9-T2A-puro and hU6-
578 gRNA expression cassettes flanked by piggyBac transposon terminal repeat elements
579 (pBACON-puro), which allows subcloning of annealed oligos containing gRNA
580 sequence at *BbsI* site, has been previously described (Shao et al., 2017b; Townshend

581 et al., 2020; Wang et al., 2021). gRNA targeting genomic sites and oligo sequences to
582 generate pBACON-GFP-h*GATA3* (primers: CRISPR_hGATA3_CDS1#1_s and
583 CRISPR_hGATA3_CDS1#1_as) and -h*TFAP2A* (CRISPR_hTFAP2A_CDS2_s and
584 CRISPR_hTFAP2A_CDS1_as) are found in **Fig. S4** and **Table 3B**; these were
585 designed using publicly available tools (http://crispr.mit.edu or
586 https://www.idtdna.com/site/order/designtool/index/CRISPR_CUSTOM).
587
588 *piggyBac-based transgenic and genome edited hESC lines*
589 PB constructs (3μg) and pCAG-ePBase (Lacoste et al., 2009) (1μg) were co-transfected
590 into H9 hESC (70,000 cells cm^{-2}) using GeneJammer transfection reagent (Agilent
591 Technologies). To enrich for successfully transfected cells, drug selection (puromycin,
592 2μg/mL for 4 days; neomycin, 250μg/mL for 5 days) was performed 48 to 72 hours after
593 transfection. hESC stably expressing each construct maintained the expression of
594 pluripotency markers. For inducible constructs, doxycycline (DOX, 500ng/mL) treatment
595 was performed for 48 hours for neomycin-selected *TFAP2A*-KO rescue pools using PB-
596 TA-ERN-hTFAP2A(CR)-HA. The TFAP2A gRNA targeted site of human TFAP2A
597 construct (gift of Robert Tjian, Addgene #12100, (Williams and Tjian, 1991)) was
598 mutated using Q5 site directed mutagenesis kit (NEB, primers: SP (RSV) AP2
599 (hTFAP2A)-CRISPR RES-fw and SP (RSV) AP2 (hTFAP2A)-CRISPR RES-rv). This
600 CRISPR resistant human TFAP2A construct was then PCR amplified (using primers:
601 Clo-dTOPO-hTFAP2A-CRISPR res-fw v2 and Clo-dTOPO-hTFAP2A-CRISPR res-rv
602 v2, HA tagging at C-terminus), which was then cloned into pENTR-dTOPO (Thermo) for
603 Gateway cloning into PB-TA-ERN (Knut Woltjen, Addgene #80474, (Kim et al., 2016))

604 to generate PB-TA-ERN-hTFAP2A(CR)-HA. Additional plasmid and primer information
605 is found in **Table 3**.
606 During pBACON-based genome editing, puro-selected cells were cultured at low
607 density (300 cells cm^{-2}) for clonal selection. Established colonies were manually picked
608 and expanded for screening indel mutations using PCR amplification of a region
609 spanning the targeted gRNA region (genomic DNA isolated using DirectPCR Lysis
610 Reagent (Tail) (VIAGEN), primers: hGATA3, PCR_GATA3_RI_fw#2 and
611 PCR_GATA3_NI_rv#2; hTFAP2A, PCR_TFAP2A_RI_fw and PCR_TFAP2A_NI_rv),
612 which were subcloned into pPBCAG-GFP (Chen and LoTurco, 2012) at EcoRI and NotI
613 sites, and sequenced (Seq-3'TR-pPB-Fw). At least 12 to 15 bacterial colonies were
614 sequenced to confirm genotypic clonality. Western blots for each protein were also
615 performed to further validate the KO lines. Control cells are H9 hESC in all loss-of-
616 function experiments.
617
618 *Western blot*
619 SDS PAGE gels (10%) and PVDF membranes were used. Membranes were blocked
620 using Intercept (TBS) Blocking Buffer (Licor), total protein quantification was performed
621 by using Revert 700 Total Protein Stain (Licor), and primary antibody overnight
622 incubation was performed at 4˚C, followed by 30-min IRDye (Licor) secondary antibody
623 incubation at room temperature. Blots were imaged using Licor Odyssey Infared
624 Imaging system.
625
626 *Immunostaining*

627 hPSC staining protocols have been previously described (e.g., (Hamed et al., 2023;
628 Shao et al., 2017a; Wang et al., 2021)). In short, samples (hPSC-cysts, hPSC-amnion)
629 grown on the coverslip were rinsed with phosphate-buffered saline (PBS; Gibco) twice,
630 fixed with 4% paraformaldehyde (Sigma-Aldrich) in 1x PBS for 40 to 60 min, then rinsed
631 with PBS three times, and permeabilized with 0.1% SDS (Sigma-Aldrich) solution for 40
632 min. The samples were blocked in 4% heat-inactivated goat serum (Gibco) or 4%
633 normal donkey serum (Gibco) in PBS 1 hour to overnight at 4°C. The samples were
634 incubated with primary antibody solution prepared in blocking solution at 4°C overnight,
635 washed three times with PBS (10 min each), and incubated in blocking solution with
636 goat or donkey raised Alexa Fluor–conjugated secondary antibodies (Thermo Fisher
637 Scientific) at room temperature for 2 hours. DNA counterstaining was performed using
638 Hoechst 33342 (nucleus, Thermo Fisher Scientific), Alexa Fluor–conjugated WGA
639 (membrane, Thermo Fisher Scientific). All samples were mounted on slides using 90%
640 glycerol (in 1x PBS). When mounting cyst samples, modeling clays were used as
641 spacers between coverslips and slides to preserve lumenal cyst morphology.
642
643 *Confocal microscopy, live imaging and image analysis*
644 Confocal Images of fixed samples were acquired using Zeiss LSM980 microscope.
645 Measurements of cell nucleus dimensions, cyst epithelial thickness, and cyst orientation
646 angle were performed manually using the Measurement tool in ImageJ (NIH).
647
648 *RNA isolation and qRT-PCR analysis*

649 Total RNA extraction was performed using TRIzol (Thermo Fisher). The quantity and
650 quality of total RNA was determined by spectrometry and denaturing agarose gel
651 electrophoresis, respectively. The cDNA was synthesized from total RNA (1μg) using
652 High-Capacity cDNA Reverse Transcription Kit (Applied Biosystems). Quantitative real-
653 time RT-PCR (qPCR) analysis of mRNA expression was performed using a CFX96
654 Real-Time PCR Detection System (BioRad) with Power Up™ SYBR Green Master Mix
655 (Applied Biosystems). Primers (**Table 3B**) were designed using NCBI primer design tool
656 to span at least one exon/intron junction. Data were normalized against *GAPDH* and are
657 shown as the average fold increase ± standard error of the mean (SEM) with relative
658 expression being calculated using the 2-ΔΔCT method as described previously (Livak
659 and Schmittgen, 2001). After amplification, the specificity of the PCR was determined by
660 both melt-curve analysis and gel electrophoresis to verify that only a single product of
661 the correct size was present.
662
663 *RNA sequencing and bioinformatics*
664 The quality of total RNA was determined using TapeStation RNA ScreenTape. RNA
665 was enriched for mRNA using NEBNext Poly(A) mRNA Magnetic Isolation Module
666 (E7490). cDNA and library preparation were performed using NEBNext® Ultra™ II
667 Directional RNA Library Prep kit for Illumina (New England Biolabs). Library
668 concentration was determined using NEBNext® Library Quant Kit for Illumina (New
669 England Biolabs) or by Qubit (Thermo). Samples were then pooled and were
670 sequenced using Illumina sequencers: NextSeq550 (Versiti Blood Research Institute) or
671 using NovaSeq 6000 (S4 flowcell, the DNA services laboratory of the Roy J. Carver

672 Biotechnology Center at the University of Illinois at Urbana-Champaign). Sequence data
673 was analyzed using the RNA-Seq workflow in Partek Flow software (Partek Inc., St.
674 Louis, MO, USA). Raw sequencing reads were mapped to the human genome hg38
675 using STAR version 2.7.8a with default parameter settings. Aligned reads were then
676 quantified to Ensembl Transcripts release 104 using Partek's method and genes with
677 fewer than 10 reads in all samples were excluded from the subsequent analyses. Gene
678 counts were then filtered based on gene_biotype for protein_coding genes, followed by
679 excluding features where maximum <= 30.0 reads. Gene expression was then
680 normalized using DESeq2 (Median Ratio). Differentially expressed genes were selected
681 using as criteria FDR < 0.05 and absolute fold change > 2.
682
683 *GO enrichment analysis*
684 GO analysis were performed on significantly upregulated (1,820) or downregulated
685 (2,092) genes in Glass-3D^{+BMP} amnion-cysts vs Glass-3D pluripotent-cysts (From **Fig.**
686 **3**).
687
688 *Mapping and gene expression analyses of Tyser et al. Carnegie Stage 7 human embryo*
689 *single cell RNA sequencing dataset*
690 The original UMAP coordinates and annotations for all 1,195 cells were used
691 throughout. The processed data were downloaded from http://www.human-gastrula.net,
692 which was used to generate a UMAP plot (using DimPlot in R package Seurat), as well
693 as to perform expression analyses (FeaturePlot in Seurat).
694

695 *Integration and gene expression analyses of Yang et al. GD14 cynomolgus macaque*
696 *embryo single cell RNA sequencing dataset*
697 The processed data were downloaded from GSE148683, and the ensemble genome
698 build Macaca_fascicularis_5.0 release 96 was used to identify human orthogonal gene
699 symbols. Datasets from two distinct GD14 embryos (Yang et al., 2021) were integrated
700 using 5,000 anchor features and 10 dimensions in the IntegrateData function in Seurat
701 R package (v.4.2.1) package: trophoblast cells were removed from the dataset prior to
702 integration. Six general cell populations (epiblast, transition, mesoderm, amnion,
703 endoderm and extraembryonic mesenchyme) were identified using FindClusters
704 function (resolution as 0.4).
705
706 *RNA velocity (scvelo) analysis of Tyser et al. Carnegie Stage 7 human embryo single*
707 *cell RNA sequencing dataset*
708 RNA velocities across all 1,195 single cells were embedded on the original UMAP
709 coordinates shown in Tyser *et al.* (Tyser et al., 2021). The Tyser et al. Carnegie Stage 7
710 human embryo raw fastq dataset was obtained from ArrayExpress (accession code: E-
711 MTAB-9388). From the aligned BAM files, a loom file was generated using the function
712 run_smartseq2 mode in software velocyto (v0.17) with default parameters to create a
713 count matrix made of spliced and unspliced read counts (with Human genome
714 annotation hg19). scVelo (Python package v.0.2.5 (Bergen et al., 2020) was used to
715 examine inferred RNA velocity and visualized the velocities on the UMAP embedding by
716 stream plot (with default parameters except smooth was set to 1).
717

718 *Transcriptomic similarity analysis between bulk RNA sequencing and Tyser et al.*
719 *Carnegie Stage 7 human embryo or Yang et al. GD14 cynomolgus macaque peri-*
720 *gastrula single cell RNA sequencing datasets*
721 Transcriptomic similarities between bulk RNA sequencing samples and the Tyser *et al.*
722 dataset were examined and visualized using original UMAP coordinates from Tyser *et*
723 *al.*. In summary, each bulk RNA-seq sample was first downsampled to 100 pseudo-
724 single cell data using R package projectLSI (Granja et al., 2019), which was followed by
725 data integration with Tyser *et al.* dataset in UMAP dimension reduction space. A medoid
726 from 100 pseudo-single cell data was used as the representation of each bulk RNA-seq
727 sample, and, for each sample, we identified the most transcriptomically similar cell from
728 Tyser *et al.* dataset, based on Euclidean distance on UMAP space. Identical
729 approaches were used for the Yang *et al.* dataset (Yang et al., 2021), except that the
730 UMAP coordinates were identified using the Seurat package as described above.
731
732 *Data availability*
733 The raw data, unfiltered count matrix and processed count matrix will be available to the
734 database of Genotypes and Phenotypes (dbGaP) upon publication.
735
736 *Statistical analyses*
737 Graphs were generated using Prism 7 (GraphPad Software) or R,
738 and statistical analyses were performed using Prism 7. Fig. 1D, 5 independent samples
739 were counted at each timepoint (total of > 50 cells/sample). For analysis we used one-
740 way ANOVA with post-hoc Dunnet's multiple comparisons test. In Fig. 1K, 3

741 independent samples were counted (total of > 75 cells were plotted). For analysis we
742 used two-tail Student-T test. In Fig. 1J, 3 independent samples were counted (total of >
743 50 cells were plotted). For analysis we used one-way ANOVA with post-hoc Tukey's
744 multiple comparison test. In Fig. 2, relative mRNA expression was detected in n=3 for
745 each timepoint. For analysis we used one-way ANOVA with post-hoc Tukey's multiple
746 comparison test. *, significant (p-value<0.05); ns, non-significant. All experiments were
747 repeated at least three times.
748

749 **FIGURE LEGENDS**

750 **Figure 1. Highly penetrant amniogenesis in a Glass-3D^{+BMP} culture system.** (**A,B**)
751 hPSC-derived pluripotent cyst (hPSC-pluripotent cyst, Glass-3D in (**A**)) and amnion cyst
752 (Glass-3D^{+BMP} in (**B**)) assays: IF images show hPSC-pluripotent (**A**) and -amnion (**B**)
753 cysts stained for PODXL (lumen, magenta) and DNA (nuclear shape, blue). BMP4
754 treatment (20ng/mL) leads to uniformly squamous amnion cysts by Day 4. (**C**) Confocal
755 optical sections of d2 cysts harvested prior to (0-min) and 10-, 20-, 30- and 60-min after
756 BMP4 treatment, stained with indicated markers. Staining for phosphorylated SMAD1/5
757 reveals a prominent nuclear pSMAD1/5 enrichment within 10-min of BMP4 treatment in
758 all cells. (**D**) Quantification of nuclear pSMAD1/5: five independent samples were
759 counted, more than 50 cells were counted per sample. * indicates statistically significant
760 changes (p<0.05) compared to 0-min timepoint. (**E**) Abundant GATA3 expression (in
761 green), but not TFAP2A (red), is seen by 3 hours after BMP4 treatment while SOX2
762 expression is maintained. (**F-H**) Pluripotency (NANOG, SOX2) and amnion (ISL1/2,
763 GATA3, TFAP2A) marker expression analyses of d4 cysts grown in the Glass-3D (top)

764 or in Glass-3D^{+BMP} (bottom) conditions. (**I,J**) Confocal micrographs of d4 cysts grown in
765 the Glass-3D^{+BMP} system stained for phosphorylated EZRIN, RADIXIN and MOESIN
766 (pERM), an apical membrane marker, as well as with indicated amnion markers (top –
767 cysts were treated with BMP4 for 24 hours between d2 and d3; bottom – treated with
768 BMP4 for 48 hours from d2 to d4). (**K,L**) Quantification of GATA3 and ISL1/2
769 fluorescent intensities in 24- (blue, n = 115 cells) and 48-hr (red, n = 76 cells) BMP4
770 treatment samples (**K**), as well as of nuclear aspect ratios of d4 hPSC-cyst (black, n =
771 63 cells), and 24- (blue, n = 45 cells) and 48-hr (red, n = 52) BMP4-treated cysts
772 (harvested at d4), (**L**). (**M**) pSMAD1/5 staining (green) shows similar nuclear enrichment
773 between 24- and 48-hr BMP4 treatment at d4 (also stained with indicated markers).
774 Scale bars = 50μm.
775
776 **Figure 2. Time-course analysis of Glass-3D^{+BMP} hPSC-amnion development.** (**A**)
777 Timeline of the Glass-3D^{+BMP} hPSC-amnion assay. Twenty four-hr BMP treatment is
778 sufficient to generate uniformly squamous hPSC-amnion cysts. (**B,C**) Optical sections of
779 time-course Glass-3D^{+BMP4} hPSC-amnion cysts (harvested at indicated timepoints after
780 BMP4 treatment) stained with indicated markers (inverted black and white fluorescent
781 signals shown for individual channels, to aid visualization). GATA3, an immediate BMP
782 target is seen by 3-hr (yellow arrowheads). hPSC-amnion cysts with prominent nuclear
783 TFAP2A (**B**) and ISL1/2 (**C**) are seen by 12- and 24-hr, respectively (yellow
784 arrowheads), while SOX2 shows gradual decrease. Consistent changes are also
785 observed at mRNA transcript levels using quantitative RT-PCR (**D-F**, also see the
786 expression of additional markers: *HAND1* (amniotic) and *NANOG* (pluripotent); *

787 indicates statistically significant changes ($p<0.05$) compared to 0-hr timepoint). (**G**)
788 Relative mRNA expression analyses of indicated pluripotency (top) and amniotic
789 (bottom) markers between d4 Glass-3D hPSC-pluripotent cyst (black), and d4 Glass-
790 3D^{+BMP} hPSC-amnion with 24-hr (blue) or 48-hr (red) BMP treatment; * indicates
791 statistically significant changes ($p<0.05$). (**H**) BMP inhibitor (LDN-193189) treatment
792 outline as well as confocal micrographs of d4 Glass-3D^{+BMP} hPSC-amnion (top, control
793 – 24-hr BMP4 treatment between d2 and d3) and hPSC-amnion treated with LDN-
794 193189 between d3 and d4 after BMP4 treatment (between d2-d3). Scale bars = 50μm.
795
796 **Figure 3. Temporally-resolved transcriptomic characterization of Glass-3D^{+BMP}**
797 **hPSC-amnion.** (**A**) Experimental timeline (from d2) of the time-course bulk RNA
798 sequencing analysis. Colored arrowheads indicate timepoints at which samples were
799 harvested. (**B**) A heatmap showing a hierarchical clustering analysis of all detected
800 genes (12,940): bulk transcriptomes from triplicate samples are shown at each
801 timepoint. A gradient scale indicates Z-score. (**C**) Principal component analysis (PCA)
802 plot of time-course bulk transcriptomes, using the most variable genes, revealing
803 progressive transcriptomic changes overtime (indicated by the dotted arrow). Note that
804 coloring is consistent with the arrowheads in (**A**). (**D**-**G**) Time-course plots of normalized
805 expression values for selected known immediate BMP target (**D**), general amnion (**E**),
806 advanced amnion (**F**) and pluripotency genes (**G**). (**H**) A volcano plot analysis showing
807 up- (red) and down- (blue) regulated genes in Glass-3D^{+BMP} hPSC-amnion cysts (gene
808 expression compared to d4 pluripotent hPSC-cysts): black lines represent cutoffs for p-
809 value <0.05 and 2-fold difference.

810

811 **Figure 4. Transcriptome comparison of developing Glass-3D^{+BMP} hPSC-amnion**
812 **cysts, a Carnegie stage (CS) 7 human embryo, and two GD14 cynomolgus**
813 **macaque peri-gastrula.** (**A**) A UMAP plot displaying the original single cell
814 transcriptome coordinates of the CS7 human embryo described in Tyser *et al.*, shown
815 with the original annotations. The inset (**i**) is used for expression analyses in (**B**). (**B**)
816 Expression of amnion markers – *GATA3*, *TFAP2A* and *ISL1* – superimposed onto the
817 UMAP plot in (**A** – **i**). (**C**) Transcriptome similarity analysis comparing the CS7 human
818 embryo single cell dataset and the Glass-3D^{+BMP} time-course bulk RNA-seq dataset,
819 showing the human CS7 embryo UMAP plot (inset) with colored cells that are
820 transcriptomically similar to each timepoints as indicated (orange – pluripotent
821 cysts/monolayer and 0-, 0.5-, 1-, 3- and 6-hr post-BMP4; green – 12-hr post-BMP4; blue
822 – 24-hr; magenta – 48-hr). While pluripotent and earlier timepoints (orange colored
823 cells) overlaps with Epiblast cells, some 12-hr (green) and all 24-hr (blue) samples are
824 similar to a subpopulation of Primitive Streak cells, and 48-hr (magenta) samples
825 overlap exclusively with Ectoderm (see Materials and Methods for detailed
826 bioinformatics pipeline). (**D**) *TBXT* expression transposed onto the CS7 human embryo
827 UMAP plot, revealing *TBXT*^{low} sub-population that show transcriptomic similarities to 24-
828 hr post-BMP samples (indicated by dotted circle). (**E**) An integrated UMAP plot for two
829 *in vitro* cultured gestation date (GD) 14 (8 days after culturing 6-day old blastocyst)
830 cynomolgus macaque peri-gastrula (replotted and reclustered from Yang *et al.*). (**F**)
831 Transcriptome similarity analysis comparing the GD14 cynomolgus macaque peri-
832 gastrula dataset and the Glass-3D^{+BMP} time-course dataset, showing the Yang *et al.*

833 GD14 UMAP plot (inset "**i**") with colored cells that are transcriptomically similar to each
834 timepoints as indicated (orange – pluripotent cysts/monolayer and 0-, 0.5-, 1-, 3-, 6- and
835 12-hr post-BMP4; blue – 24-hr; magenta – 48-hr). While pluripotent and early datapoints
836 (orange colored cells) overlap with epiblast cells, the 24-hr samples share similarities
837 with *TBXT*^{low} population, and the 48-hr samples overlap with ISL1^{high} amnion cells ((**G**),
838 expression analysis of indicated markers). Gradient scales indicate expression level
839 (orange = high, gray = low). Uncropped plots are found in **Fig. S2**.
840
841 **Figure 5. Transcriptional characterizations of amnion-epiblast squamocolumnar**
842 **boundary of the CS6/7 cynomolgus monkey amniotic sac.** (**A**) RNA velocity
843 analysis (scvelo) of the *Tyser et al.* CS7 human embryo dataset, showing predicted
844 lineage progression trajectories from Epiblast to Ectoderm traversing the *TBXT*^{low}
845 population. (**B-G**) Optical sections of a CS6/7 cynomolgus macaque embryo stained for
846 indicated transcription factors (GATA3, ISL1/2, pSMAD1/5 and SOX2 (**B**,**D**,**F**)), as well
847 as quantitation for relative fluorescent intensity in proximal (closer to epiblast) to distal
848 (closer to amnion) cells of indicated markers at the amnion-epiblast boundary (**C**, **E** and
849 **G** are quantitation of images in **B**, **D** and **F**, respectively). Each dot represents a single
850 cell. (**i**), (**ii**) and (**iii**) indicate insets in (**F**). Half of the amniotic sac shown. Quantitation
851 shows that, while GATA3^{+}/TFAP2A^{+} cells are also SOX2^{+}, ISL1^{+} cells are only seen
852 after SOX2 expression is no longer detected: ISL1 expression is exclusive to squamous
853 amnion cells. Moreover, the expression of pSMAD1/5 and TFAP2A is reduced in most
854 distal amnion (**ii**, **iii**). Scale bars 200μm. (**H**) Nuclear aspect ratio quantitation of amnion-
855 epiblast boundary cells in (**B**), (**C**) and (**D**), mean+SEM shown. Dotted vertical line in

856 each plot indicates amnion-epiblast boundary (**C**,**E**,**G**,**H**). (**I**) A schematic representation
857 of the CS6/7 cynomolgus macaque amniotic sac: the confocal micrographs in (**B**) were
858 edited to represent SOX2^{+} epiblast (pseudocolored in blue), primitive streak-derived
859 disseminating (green), GATA3^{+}/TFAP2A^{+}/SOX2^{low} transition boundary (magenta) and
860 GATA3^{+}/TFAP2A^{+}/ISL1^{+} lineage specified amnion (red) cells.
861
862 **Figure 6. Characterization of differentially expressed genes identified through the**
863 **Glass-3D^{+BMP} hPSC-amnion time-course sequencing analysis.** (**A-E**) Combined and
864 selected genes are shown for each category (A – immediate; B – early; C –
865 intermediate-1; D – intermediate-2; E – late). Genes for each category are selected
866 based on significant upregulation (FDR<0.05, fold>2, based on Z-scores) by 1-
867 (immediate, n = 5), 3- (early, n = 9), 6- to 12- (intermediate-1, n = 30), 24- (intermediate-
868 2, n = 178) and 48-hr (late, n = 157) post-BMP4 treatment, compared to the previous
869 timepoint. Vertical lines indicate timepoints at which significant changes are seen.
870
871 **Figure 7. Establishment of DLX5 as a new marker of amniogenesis similar to**
872 **TFAP2A.** (**A,B**) Expression analyses for *ISL1* (**A**) and *DLX5* (**B**) in the time-course bulk
873 RNA sequencing (top) and in the single cell CS7 human embryo (bottom) datasets. (**C**)
874 Confocal optical sections of Glass-3D^{+BMP4} hPSC-amnion cysts (at 0-hr, 24-hr (d3) and
875 d4) stained with indicated markers. (**D**) Histological section of a cynomolgus monkey
876 amniotic sac at CS7 stained with indicated markers (SOX2^{+} epiblast;
877 TFAP2A^{+}/DLX5^{+}/SOX2^{-} amnion). Insets (**i** and **ii**) indicate the amnion-epiblast
878 boundaries. DLX5 and TFAP2A share a similar expression pattern at the boundary.

879 Similar to pSMAD1/5 and TFAP2A (shown in **Fig. 5F**), most distal amnion cells show
880 reduced DLX5 expression. Surface ectoderm bridging neural ectoderm and amniotic
881 ectoderm is not seen at this stage. Amniotic mesenchyme is observed underlying the
882 TFAP2A^{+}/DLX5^{+} amniotic epithelium at this stage. Scale bars = 500μm.
883
884 **Figure 8. Analyses of Glass-3D^{+BMP} hPSC-amnion in control and *TFAP2A*-KO**
885 **background.** (**A,B**) Optical sections of control and *TFAP2A*-KO cysts in Glass-3D (**A**,
886 pluripotent) as well as in Glass-3D^{+BMP} (**B**). While control-like pluripotent cysts are
887 formed in Glass-3D, several NANOG^{+} cells are still seen in Glass-3D^{+BMP} in the
888 absence of *TFAP2A*. (**C**) Confocal micrographs of d4 control, *TFAP2A*-KO and
889 *TFAP2A*-KO carrying a DOX-inducible human TFAP2A transgenic construct with or
890 without DOX treatment, stained with indicated markers. (**D**) Transcriptome similarity
891 analysis comparing the CS7 human embryo single cell dataset with the time-course (0-,
892 12-, 24- and 48-hr post-BMP) bulk dataset from control and *TFAP2A*-KO Glass-3D^{+BMP}
893 hPSC-amnion. Orange, green, blue and magenta colored cells are transcriptomically
894 similar to 0-, 12-, 24- and 48-hr post-BMP bulk RNA sequencing samples, respectively.
895 While a clear differentiation trajectory from Epiblast to Ectoderm is seen in control (left),
896 a halted amnion lineage progression is seen in the *TFAP2A*-KO background. (**E**) Optical
897 sections of control and *TFAP2A*-KO cysts in Glass-3D^{+BMP} stained for NANOG (green),
898 ISL1/2 (red) and TBXT (magenta). Scale bars = 50μm.
899
900 **Table 1. Glass-3D^{+BMP} hPSC-amnion time-course bulk RNA sequencing dataset.**

901 (**A**) normalized and filtered count matrix of the time-course bulk-RNA sequencing. (**B-C**)
902 Gene expression comparison analysis between 48-hr (d4) Glass-3D^{+BMP} hPSC-amnion
903 and d4 Glass-3D hPSC-cysts: lists of 1,813 up-regulated (**B**) and 2,088 down- (**C**)
904 regulated genes. (**D-E**) Gene Ontology analyses (Biological Processes) for top all
905 significantly up- (**D**) and down- (**E**) regulated genes.
906
907 **Table 2. Lists of immediate, early, intermediate and late genes.** An excel file
908 containing temporally resolved gene lists: (**A**) immediate (0.5- and 1-hr, 57 genes); (**B**)
909 early (3- and 6-hr, 135 genes); (**C**) intermediate-1 (12-hr, 81 genes); (**D**) intermediate-2
910 (24-hr, 642 genes); (**E**) late (48-hr, 909 genes). Genes that showed significant
911 upregulation compared to the previous timepoint (e.g., 0.5-hr compared to 0-hr, 3-hr
912 compared to 1-hr) were retained. Duplicated genes found in the list from earlier
913 timepoint lists are removed. For example, *GATA3* is significantly upregulated throughout
914 the time course, but is only included in the immediate category. Genes with averaged
915 normalized counts < 100 were excluded.
916
917 **Table 3. Lists of reagents used in this study.** (**A-C**) Lists of antibodies (**A**), primers
918 (**B**) and plasmids (**C**).
919
920 **Movie 1. All optical sections of Glass-3D^{+BMP} hPSC-amnion shown in Fig. 1B.**
921
922 **SUPPLEMENTARY FIGURE LEGENDS**

923 **Figure S1. Glass-3D^{+BMP} hPSC-amnion formation using 1196a human induced**
924 **pluripotent stem cell and H7 human embryonic stem cell lines.** (**A-C**) Confocal
925 micrographs of 1196a (**A,B**) and H7 lines (**C**) grown in the Glass-3D^{+BMP} condition,
926 stained with indicated markers and timepoints. Scale bars = 50μm.
927
928 **Figure S2. Original UMAP plots and TBXT expression analyses.** (**A,B**) Original
929 UMAP expression plots of the Tyser *et al.* CS7 human embryo single cell RNA
930 sequencing dataset used in this study (*GATA3*, *TFAP2A*, *ISL1, TBXT* and *DLX5*, **A**) as
931 well as time-course transcriptome similarity UMAP plot (**B**). (**C**) Confocal micrographs of
932 control Glass-3D^{+BMP} cysts stained for ISL1/2 (green), SOX2 (red) and TBXT (magenta).
933 (**D**) Time-course plot of normalized expression values for *TBXT*. (**E,F**) Original time-
934 course transcriptome similarity UMAP plot of the Yang *et al.* GD14 cynomolgus
935 macaque dataset (**E**) as well as expression plots (**F**). (**G**) Optical sections of a CS6/7
936 cynomolgus macaque embryo stained for TBXT and SOX2. TBXT expression is
937 enriched in primitive streak as well as in the primitive streak-derived disseminating cells.
938
939 **Figure S3. Quantitation for relative fluorescent intensity in proximal and distal**
940 **cells of indicated markers at the amnion-epiblast boundary in a CS7 cynomolgus**
941 **macaque embryo.**
942
943 **Figure S4. Validation of *GATA3*- and *TFAP2A*-KO hPSC lines.** (**A-C**) Sequenced
944 genotyping results of *GATA3*-KO #1 and #2 lines (**A**), representative sequence traces
945 for each mutations are shown in (**B**). Western blot analysis for GATA3 in control and

946 *GATA3*-KO #1 and #2 lysates (**C**, β-ACTIN is used as a loading control, triplicates
947 shown). (**D-F**) Genotyping results of *TFAP2A*-KO #1 and #2 lines (**D**), representative
948 sequence traces for each mutation are shown in (**E**). Western blot analysis for TFAP2A
949 in control and *TFAP2A*-KO #1 and #2 lysates (**F**, β-ACTIN is used as a loading control,
950 duplicates shown).
951
952 **Figure S5. Uncropped transcriptional similarity UMAP plots for control and**
953 ***TFAP2A*-KO shown in Fig. 8D.**
954
955 **ACKNOWLEDGEMENTS**
956 We thank K. Woltjen (Kyoto University) for the piggyBac DOX-inducible vector (PB-TA-
957 ERN, Addgene#80474), A. Brivanlou (Rockefeller University) for ePB transposase, as
958 well as Robert Tjian (University of California - Berkley) for human TFAP2A plasmid (SP
959 (RSV) AP-2, Addgene#12100). We thank Michaela Patterson, Matthew Veldman and
960 Deborah Gumucio for their insightful comments to the manuscript, as well as Versiti
961 Blood Research Institute Molecular Biology Core Lab and the DNA Services laboratory
962 of the Roy J. Carver Biotechnology Center at the University of Illinois at Urbana-
963 Champaign for sequence services. We also thank the Wisconsin National Primate
964 Research Center (WNPRC) Veterinary, Scientific Protocol Implementation, Pathology
965 and Animal Services Unit staff for providing animal care, and assisting in procedures
966 including breeding, pregnancy monitoring, and sample collection. The contents of this
967 manuscript are solely the responsibility of the authors and do not represent the official
968 views of the NIH.

Funding: This work was supported by NIH grants R01-HD098231 (K.T.) and P51-OD011106 (to the WNPRC) as well as by MCW CBNA Start-up funds (K.T.).

Competing interests: The authors declare no competing interest. **Data and materials availability**: All data needed to evaluate the conclusions in the paper are present in the paper and the Supplementary Materials. Further information and requests for reagents may be directed to Kenichiro Taniguchi.

REFERENCES

Abe, M., Cox, T.C., Firulli, A.B., Kanai, S.M., Dahlka, J., Lim, K.C., Engel, J.D., and Clouthier, D.E. (2021). GATA3 is essential for separating patterning domains during facial morphogenesis. Development *148*.

Beddington, R.S., and Robertson, E.J. (1999). Axis development and early asymmetry in mammals. Cell *96*, 195-209.

Bergen, V., Lange, M., Peidli, S., Wolf, F.A., and Theis, F.J. (2020). Generalizing RNA velocity to transient cell states through dynamical modeling. Nature biotechnology *38*, 1408-1414.

Bergmann, S., Penfold, C.A., Slatery, E., Siriwardena, D., Drummer, C., Clark, S., Strawbridge, S.E., Kishimoto, K., Vickers, A., Tewary, M.*, et al.* (2022). Spatial profiling of early primate gastrulation in utero. Nature *609*, 136-143.

Bonilla-Claudio, M., Wang, J., Bai, Y., Klysik, E., Selever, J., and Martin, J.F. (2012). Bmp signaling regulates a dose-dependent transcriptional program to control facial skeletal development. Development *139*, 709-719.

Carleton, A.E., Duncan, M.C., and Taniguchi, K. (2022). Human epiblast lumenogenesis: From a cell aggregate to a lumenal cyst. Seminars in cell & developmental biology *131*, 117-123.

Castillo-Venzor, A., Penfold, C.A., Morgan, M.D., Tang, W.W., Kobayashi, T., Wong, F.C., Bergmann, S., Slatery, E., Boroviak, T.E., Marioni, J.C.*, et al.* (2023). Origin and segregation of the human germline. Life Sci Alliance *6*.

Chen, F., and LoTurco, J. (2012). A method for stable transgenesis of radial glia lineage in rat neocortex by piggyBac mediated transposition. Journal of neuroscience methods *207*, 172-180.

Chen, H.M., DeLong, C.J., Bame, M., Rajapakse, I., Herron, T.J., McInnis, M.G., and O'Shea, K.S. (2014). Transcripts involved in calcium signaling and telencephalic neuronal fate are altered in induced pluripotent stem cells from bipolar disorder patients. Translational psychiatry *4*, e375.

Chen, K., Zheng, Y., Xue, X., Liu, Y., Resto Irizarry, A.M., Tang, H., and Fu, J. (2021). Branching development of early post-implantation human embryonic-like tissues in 3D stem cell culture. Biomaterials *275*, 120898.

1007 Enders, A.C., Hendrickx, A.G., and Schlafke, S. (1983). Implantation in the rhesus
1008 monkey: initial penetration of endometrium. The American journal of anatomy *167*, 275-
1009 298.
1010 Enders, A.C., Schlafke, S., and Hendrickx, A.G. (1986). Differentiation of the embryonic
1011 disc, amnion, and yolk sac in the rhesus monkey. The American journal of anatomy
1012 *177*, 161-185.
1013 Granja, J.M., Klemm, S., McGinnis, L.M., Kathiria, A.S., Mezger, A., Corces, M.R.,
1014 Parks, B., Gars, E., Liedtke, M., Zheng, G.X.Y.*, et al.* (2019). Single-cell multiomic
1015 analysis identifies regulatory programs in mixed-phenotype acute leukemia. Nature
1016 biotechnology *37*, 1458-1465.
1017 Gunne-Braden, A., Sullivan, A., Gharibi, B., Sheriff, R.S.M., Maity, A., Wang, Y.F.,
1018 Edwards, A., Jiang, M., Howell, M., Goldstone, R.*, et al.* (2020). GATA3 Mediates a
1019 Fast, Irreversible Commitment to BMP4-Driven Differentiation in Human Embryonic
1020 Stem Cells. Cell stem cell *26*, 693-706 e699.
1021 Hamed, M.M., Taniguchi, K., and Duncan, M.C. (2023). Monitoring Effects of Membrane
1022 Traffic Via Changes in Cell Polarity and Morphogenesis in Three-Dimensional Human
1023 Pluripotent Stem Cell Cysts. Methods in molecular biology *2557*, 83-98.
1024 Kim, S.I., Oceguera-Yanez, F., Sakurai, C., Nakagawa, M., Yamanaka, S., and Woltjen,
1025 K. (2016). Inducible Transgene Expression in Human iPS Cells Using Versatile All-in-
1026 One piggyBac Transposons. Methods in molecular biology *1357*, 111-131.
1027 Kinoshita, M., and Smith, A. (2018). Pluripotency Deconstructed. Development, growth
1028 & differentiation *60*, 44-52.
1029 Lacoste, A., Berenshteyn, F., and Brivanlou, A.H. (2009). An efficient and reversible
1030 transposable system for gene delivery and lineage-specific differentiation in human
1031 embryonic stem cells. Cell stem cell *5*, 332-342.
1032 Livak, K.J., and Schmittgen, T.D. (2001). Analysis of relative gene expression data
1033 using real-time quantitative PCR and the 2(-Delta Delta C(T)) Method. Methods *25*, 402-
1034 408.
1035 Miki, T., Lehmann, T., Cai, H., Stolz, D.B., and Strom, S.C. (2005). Stem cell
1036 characteristics of amniotic epithelial cells. Stem cells *23*, 1549-1559.
1037 Miki, T., and Strom, S.C. (2006). Amnion-derived pluripotent/multipotent stem cells.
1038 Stem Cell Rev *2*, 133-142.
1039 Nakamura, T., Fujiwara, K., Saitou, M., and Tsukiyama, T. (2021). Non-human primates
1040 as a model for human development. Stem cell reports *16*, 1093-1103.
1041 Nakamura, T., Okamoto, I., Sasaki, K., Yabuta, Y., Iwatani, C., Tsuchiya, H., Seita, Y.,
1042 Nakamura, S., Yamamoto, T., and Saitou, M. (2016). A developmental coordinate of
1043 pluripotency among mice, monkeys and humans. Nature *537*, 57-62.
1044 Nakamura, T., Yabuta, Y., Okamoto, I., Sasaki, K., Iwatani, C., Tsuchiya, H., and
1045 Saitou, M. (2017). Single-cell transcriptome of early embryos and cultured embryonic
1046 stem cells of cynomolgus monkeys. Scientific data *4*, 170067.
1047 Nasr Esfahani, S., Shao, Y., Resto Irizarry, A.M., Li, Z., Xue, X., Gumucio, D.L., and Fu,
1048 J. (2019). Microengineered human amniotic ectoderm tissue array for high-content
1049 developmental phenotyping. Biomaterials *216*, 119244.
1050 Rothstein, M., and Simoes-Costa, M. (2020). Heterodimerization of TFAP2 pioneer
1051 factors drives epigenomic remodeling during neural crest specification. Genome Res
1052 *30*, 35-48.

Sasaki, K., Nakamura, T., Okamoto, I., Yabuta, Y., Iwatani, C., Tsuchiya, H., Seita, Y., Nakamura, S., Shiraki, N., Takakuwa, T.*, et al.* (2016). The Germ Cell Fate of Cynomolgus Monkeys Is Specified in the Nascent Amnion. Developmental cell *39*, 169-185.

Shahbazi, M.N., Scialdone, A., Skorupska, N., Weberling, A., Recher, G., Zhu, M., Jedrusik, A., Devito, L.G., Noli, L., Macaulay, I.C.*, et al.* (2017). Pluripotent state transitions coordinate morphogenesis in mouse and human embryos. Nature *552*, 239-243.

Shahbazi, M.N., and Zernicka-Goetz, M. (2018). Deconstructing and reconstructing the mouse and human early embryo. Nature cell biology.

Shao, Y., and Fu, J. (2022). Engineering multiscale structural orders for high-fidelity embryoids and organoids. Cell stem cell *29*, 722-743.

Shao, Y., Taniguchi, K., Gurdziel, K., Townshend, R.F., Xue, X., Yong, K.M.A., Sang, J., Spence, J.R., Gumucio, D.L., and Fu, J. (2017a). Self-organized amniogenesis by human pluripotent stem cells in a biomimetic implantation-like niche. Nature materials *16*, 419-425.

Shao, Y., Taniguchi, K., Townshend, R.F., Miki, T., Gumucio, D.L., and Fu, J. (2017b). A pluripotent stem cell-based model for post-implantation human amniotic sac development. Nature communications *8*, 208.

Smith, A. (2017). Formative pluripotency: the executive phase in a developmental continuum. Development *144*, 365-373.

Takaku, M., Grimm, S.A., Shimbo, T., Perera, L., Menafra, R., Stunnenberg, H.G., Archer, T.K., Machida, S., Kurumizaka, H., and Wade, P.A. (2016). GATA3-dependent cellular reprogramming requires activation-domain dependent recruitment of a chromatin remodeler. Genome Biol *17*, 36.

Tanaka, H., Takizawa, Y., Takaku, M., Kato, D., Kumagawa, Y., Grimm, S.A., Wade, P.A., and Kurumizaka, H. (2020). Interaction of the pioneer transcription factor GATA3 with nucleosomes. Nature communications *11*, 4136.

Taniguchi, K., Heemskerk, I., and Gumucio, D.L. (2019). Opening the black box: Stem cell-based modeling of human post-implantation development. The Journal of cell biology *218*, 410-421.

Taniguchi, K., Shao, Y., Townshend, R.F., Cortez, C.L., Harris, C.E., Meshinchi, S., Kalantry, S., Fu, J., O'Shea, K.S., and Gumucio, D.L. (2017). An apicosome initiates self-organizing morphogenesis of human pluripotent stem cells. The Journal of cell biology *216*, 3981-3990.

Taniguchi, K., Shao, Y., Townshend, R.F., Tsai, Y.H., DeLong, C.J., Lopez, S.A., Gayen, S., Freddo, A.M., Chue, D.J., Thomas, D.J.*, et al.* (2015). Lumen Formation Is an Intrinsic Property of Isolated Human Pluripotent Stem Cells. Stem cell reports *5*, 954-962.

Townshend, R.F., Shao, Y., Wang, S., Cortez, C.L., Esfahani, S.N., Spence, J.R., O'Shea, K.S., Fu, J., Gumucio, D.L., and Taniguchi, K. (2020). Effect of Cell Spreading on Rosette Formation by Human Pluripotent Stem Cell-Derived Neural Progenitor Cells. Front Cell Dev Biol *8*, 588941.

Tyser, R.C.V., Mahammadov, E., Nakanoh, S., Vallier, L., Scialdone, A., and Srinivas, S. (2021). Single-cell transcriptomic characterization of a gastrulating human embryo. Nature *600*, 285-289.

Van Otterloo, E., Milanda, I., Pike, H., Thompson, J.A., Li, H., Jones, K.L., and Williams, T. (2022). AP-2alpha and AP-2beta cooperatively function in the craniofacial surface ectoderm to regulate chromatin and gene expression dynamics during facial development. eLife *11*.

Vincentz, J.W., Casasnovas, J.J., Barnes, R.M., Que, J., Clouthier, D.E., Wang, J., and Firulli, A.B. (2016). Exclusion of Dlx5/6 expression from the distal-most mandibular arches enables BMP-mediated specification of the distal cap. Proceedings of the National Academy of Sciences of the United States of America *113*, 7563-7568.

Wang, S., Lin, C.W., Carleton, A.E., Cortez, C.L., Johnson, C., Taniguchi, L.E., Sekulovski, N., Townshend, R.F., Basrur, V., Nesvizhskii, A.I.*, et al.* (2021). Spatially resolved cell polarity proteomics of a human epiblast model. Sci Adv *7*.

Williams, T., and Tjian, R. (1991). Analysis of the DNA-binding and activation properties of the human transcription factor AP-2. Genes & development *5*, 670-682.

Yang, R., Goedel, A., Kang, Y., Si, C., Chu, C., Zheng, Y., Chen, Z., Gruber, P.J., Xiao, Y., Zhou, C.*, et al.* (2021). Amnion signals are essential for mesoderm formation in primates. Nature communications *12*, 5126.

Zaret, K.S., and Carroll, J.S. (2011). Pioneer transcription factors: establishing competence for gene expression. Genes & development *25*, 2227-2241.

Zhao, C., Reyes, A.P., Schell, J.P., Weltner, J., Ortega, N.M., Zheng, Y., Björklund, Å.K., Rossant, J., Fu, J., Petropoulos, S.*, et al.* (2021). Reprogrammed blastoids contain amnion-like cells but not trophectoderm. bioRxiv, 2021.2005.2007.442980.

Zheng, Y., Xue, X., Shao, Y., Wang, S., Esfahani, S.N., Li, Z., Muncie, J.M., Lakins, J.N., Weaver, V.M., Gumucio, D.L.*, et al.* (2019). Controlled modelling of human epiblast and amnion development using stem cells. Nature *573*, 421-425.

Zheng, Y., Yan, R.Z., Sun, S., Kobayashi, M., Xiang, L., Yang, R., Goedel, A., Kang, Y., Xue, X., Esfahani, S.N.*, et al.* (2022). Single-cell analysis of embryoids reveals lineage diversification roadmaps of early human development. Cell stem cell *29*, 1402-1419 e1408.

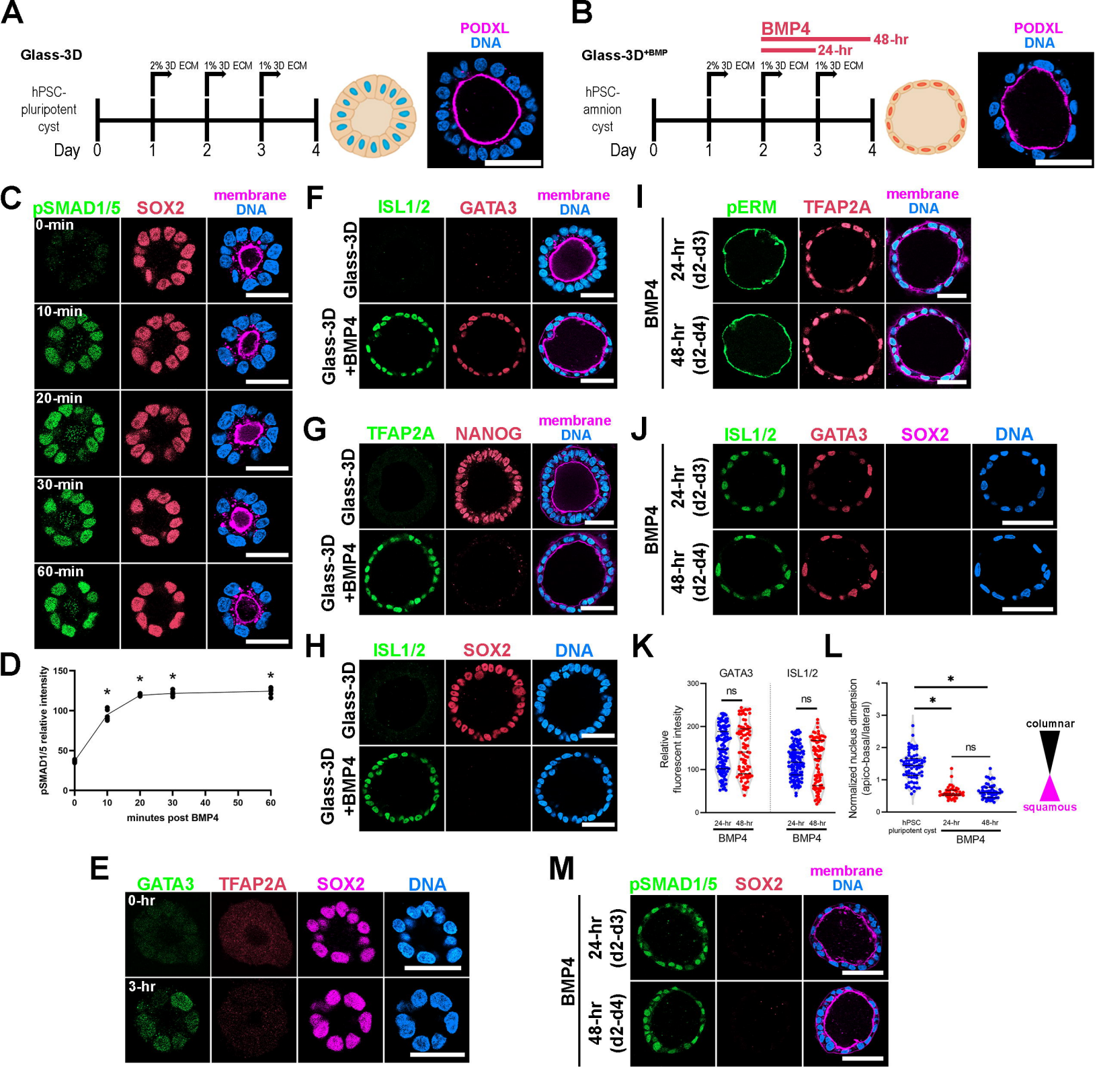
A
Glass-3D
hPSC-pluripotent cyst
2% 3D ECM
1% 3D ECM
1% 3D ECM
Day 0 1 2 3 4
PODXL
DNA
B
Glass-3D+BMP
hPSC-amnion cyst
BMP4
48-hr
24-hr
2% 3D ECM
1% 3D ECM
1% 3D ECM
Day 0 1 2 3 4
PODXL
DNA
C
pSMAD1/5
SOX2
membrane
DNA
0-min
10-min
20-min
30-min
60-min
D
pSMAD1/5 relative intensity
minutes post BMP4
E
GATA3
TFAP2A
SOX2
DNA
0-hr
3-hr
F
ISL1/2
GATA3
membrane
DNA
Glass-3D
Glass-3D +BMP4
G
TFAP2A
NANOG
membrane
DNA
Glass-3D
Glass-3D +BMP4
H
ISL1/2
SOX2
DNA
Glass-3D
Glass-3D +BMP4
I
pERM
TFAP2A
membrane
DNA
BMP4
24-hr (d2-d3)
48-hr (d2-d4)
J
ISL1/2
GATA3
SOX2
DNA
BMP4
24-hr (d2-d3)
48-hr (d2-d4)
K
GATA3
ISL1/2
ns
Relative fluorescent intesity
24-hr 48-hr
BMP4
L
Normalized nucleus dimension (apico-basal/lateral)
hPSC pluripotent cyst
24-hr
48-hr
BMP4
ns
columnar
squamous
M
pSMAD1/5
SOX2
membrane
DNA
BMP4
24-hr (d2-d3)
48-hr (d2-d4)

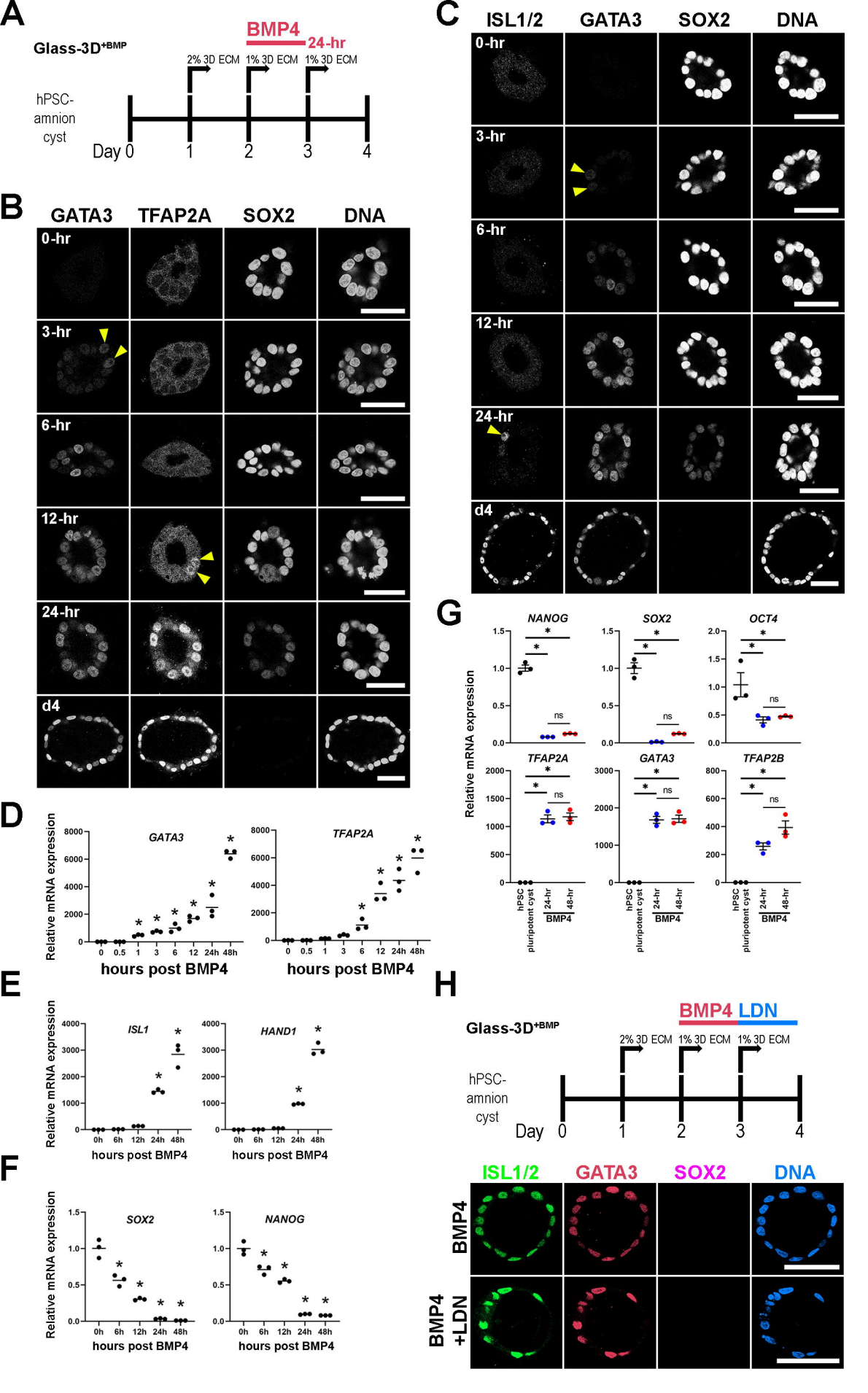
A
Glass-3D+BMP
BMP4
24-hr
2% 3D ECM
1% 3D ECM
1% 3D ECM
hPSC-amnion cyst
Day 0
1
2
3
4
B
GATA3
TFAP2A
SOX2
DNA
0-hr
3-hr
6-hr
12-hr
24-hr
d4
C
ISL1/2
GATA3
SOX2
DNA
0-hr
3-hr
6-hr
12-hr
24-hr
d4
D
GATA3
TFAP2A
Relative mRNA expression
hours post BMP4
0
0.5
1
3
6
12
24h
48h
E
ISL1
HAND1
Relative mRNA expression
hours post BMP4
0h
6h
12h
24h
48h
F
SOX2
NANOG
Relative mRNA expression
hours post BMP4
G
NANOG
SOX2
OCT4
TFAP2A
GATA3
TFAP2B
Relative mRNA expression
ns
hPSC
pluripotent cyst
24-hr
48-hr
BMP4
H
Glass-3D+BMP
BMP4
LDN
2% 3D ECM
1% 3D ECM
1% 3D ECM
hPSC-amnion cyst
Day 0
1
2
3
4
ISL1/2
GATA3
SOX2
DNA
BMP4
BMP4 +LDN

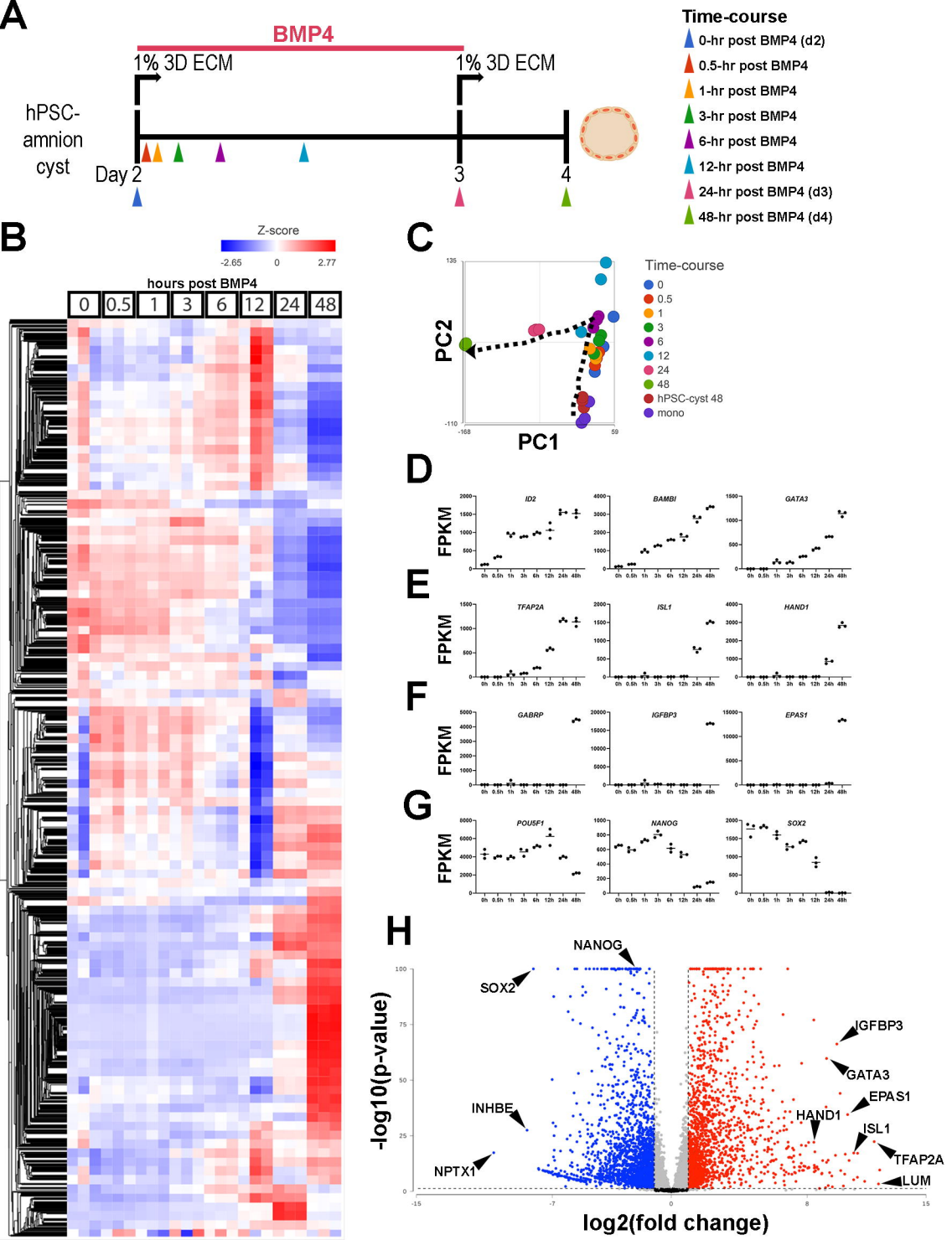
A
BMP4
1% 3D ECM
1% 3D ECM
hPSC-amnion cyst
Day 2
3
4
Time-course
0-hr post BMP4 (d2)
0.5-hr post BMP4
1-hr post BMP4
3-hr post BMP4
6-hr post BMP4
12-hr post BMP4
24-hr post BMP4 (d3)
48-hr post BMP4 (d4)
B
Z-score
-2.65
0
2.77
hours post BMP4
0
0.5
1
3
6
12
24
48
C
Time-course
0
0.5
1
3
6
12
24
48
hPSC-cyst 48
mono
PC2
PC1
D
FPKM
ID2
BAMBI
GATA3
E
FPKM
TFAP2A
ISL1
HAND1
F
FPKM
GABRP
IGFBP3
EPAS1
G
FPKM
POU5F1
NANOG
SOX2
H
NANOG
SOX2
IGFBP3
GATA3
EPAS1
HAND1
ISL1
TFAP2A
LUM
INHBE
NPTX1
-log10(p-value)
log2(fold change)

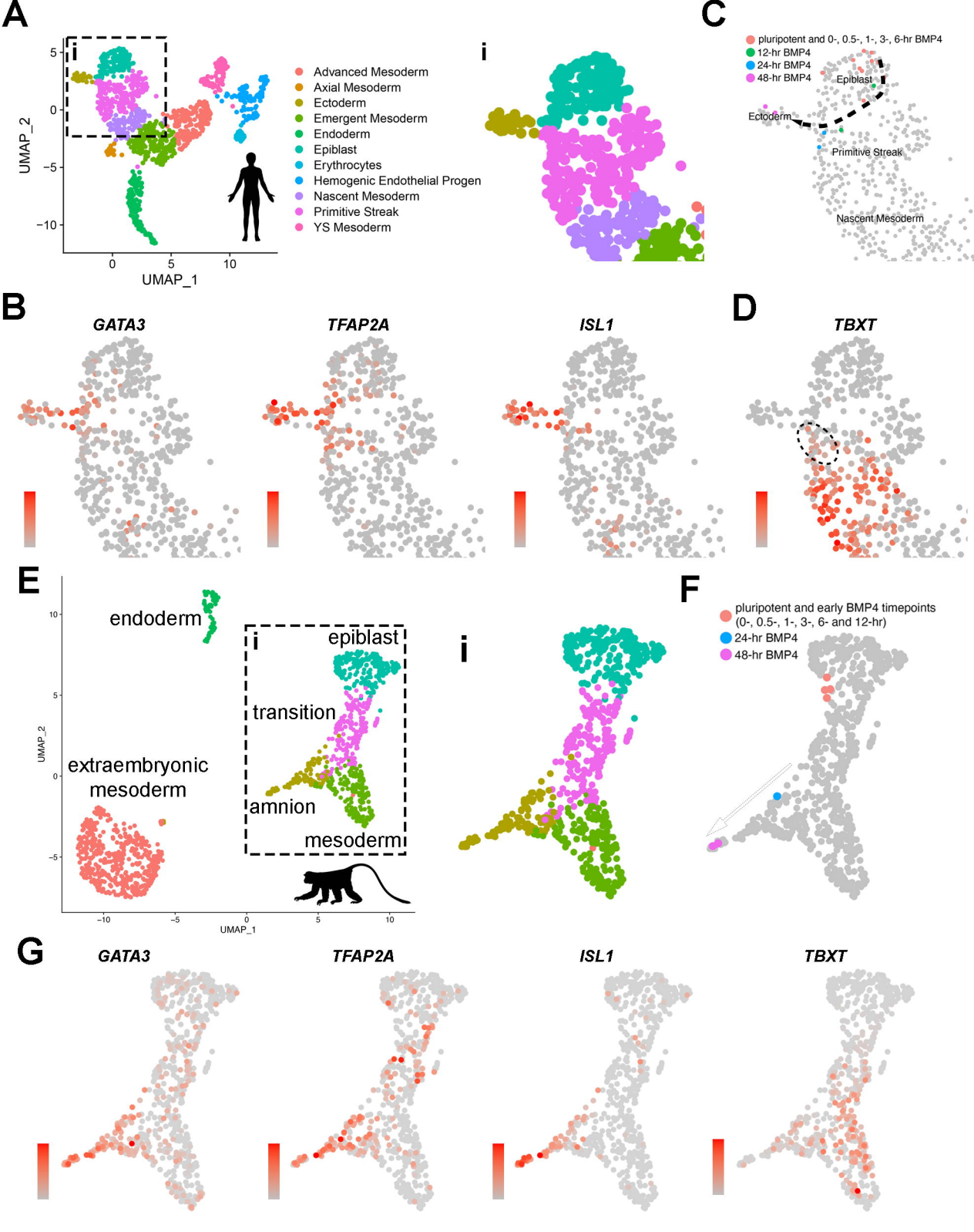
A
i
UMAP_2
UMAP_1
Advanced Mesoderm
Axial Mesoderm
Ectoderm
Emergent Mesoderm
Endoderm
Epiblast
Erythrocytes
Hemogenic Endothelial Progen
Nascent Mesoderm
Primitive Streak
YS Mesoderm
C
pluripotent and 0-, 0.5-, 1-, 3-, 6-hr BMP4
12-hr BMP4
24-hr BMP4
48-hr BMP4
Epiblast
Ectoderm
Primitive Streak
Nascent Mesoderm
B
GATA3
TFAP2A
ISL1
D
TBXT
E
endoderm
epiblast
transition
amnion
mesoderm
extraembryonic mesoderm
F
pluripotent and early BMP4 timepoints (0-, 0.5-, 1-, 3-, 6- and 12-hr)
24-hr BMP4
48-hr BMP4
G
GATA3
TFAP2A
ISL1
TBXT

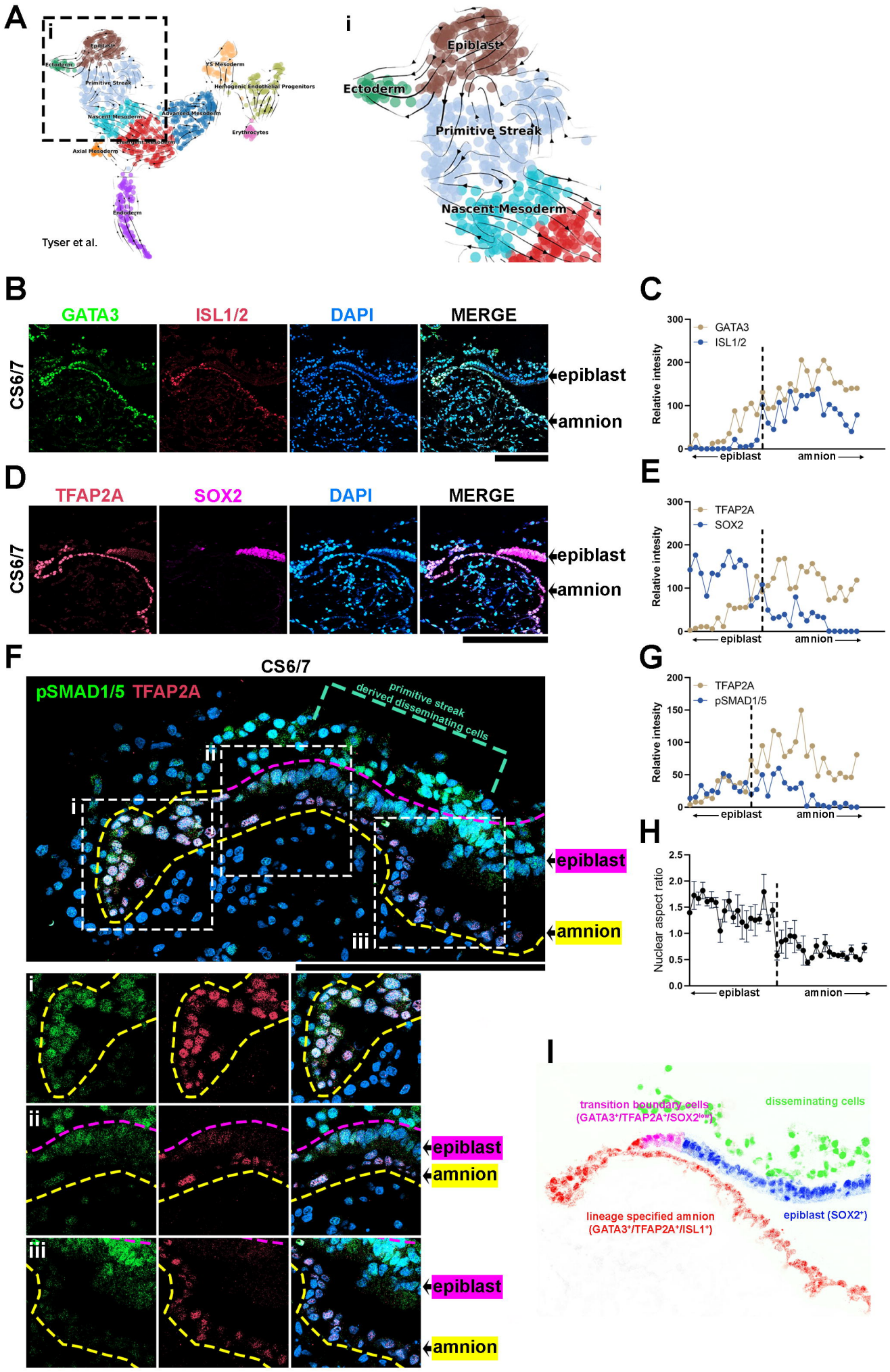
A
i
Epiblast
Ectoderm
Primitive Streak
Nascent Mesoderm
Axial Mesoderm
Endoderm
YS Mesoderm
Hemogenic Endothelial Progenitors
Erythrocytes
Tyser et al.
Epiblast
Ectoderm
Primitive Streak
Nascent Mesoderm
B
GATA3
ISL1/2
DAPI
MERGE
CS6/7
epiblast
amnion
C
GATA3
ISL1/2
Relative intesity
epiblast
amnion
D
TFAP2A
SOX2
DAPI
MERGE
CS6/7
epiblast
amnion
E
TFAP2A
SOX2
Relative intesity
epiblast
amnion
F
CS6/7
pSMAD1/5 TFAP2A
primitive streak derived disseminating cells
ii
i
iii
epiblast
amnion
G
TFAP2A
pSMAD1/5
Relative intesity
epiblast
amnion
H
Nuclear aspect ratio
epiblast
amnion
i
ii
iii
epiblast
amnion
epiblast
amnion
I
transition boundary cells
(GATA3+/TFAP2A+/SOX2low)
disseminating cells
lineage specified amnion
(GATA3+/TFAP2A+/ISL1+)
epiblast (SOX2+)

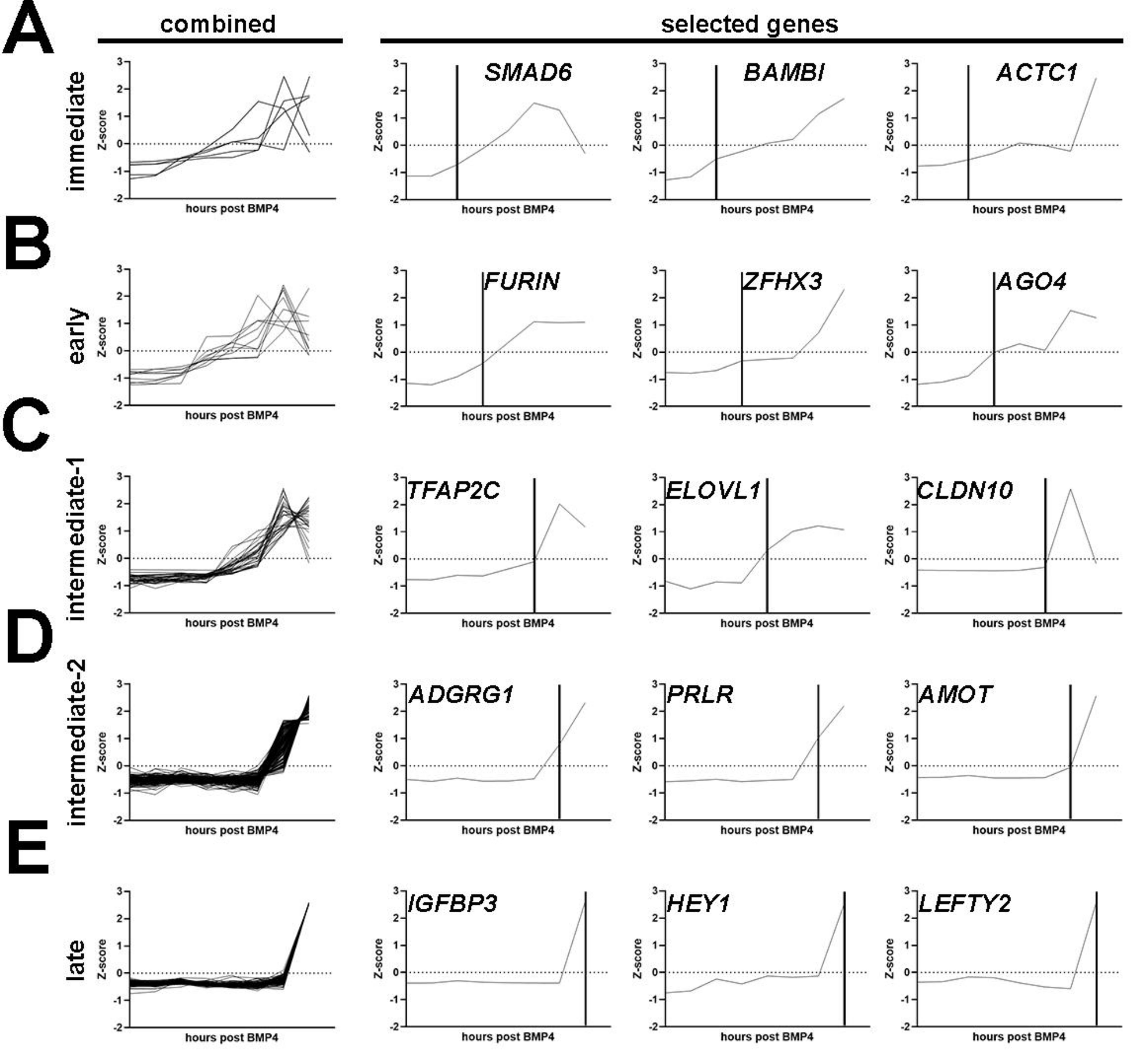
A
B
C
D
E
combined
selected genes
immediate
early
intermediate-1
intermediate-2
late
SMAD6
BAMBI
ACTC1
FURIN
ZFHX3
AGO4
TFAP2C
ELOVL1
CLDN10
ADGRG1
PRLR
AMOT
IGFBP3
HEY1
LEFTY2
Z-score
hours post BMP4

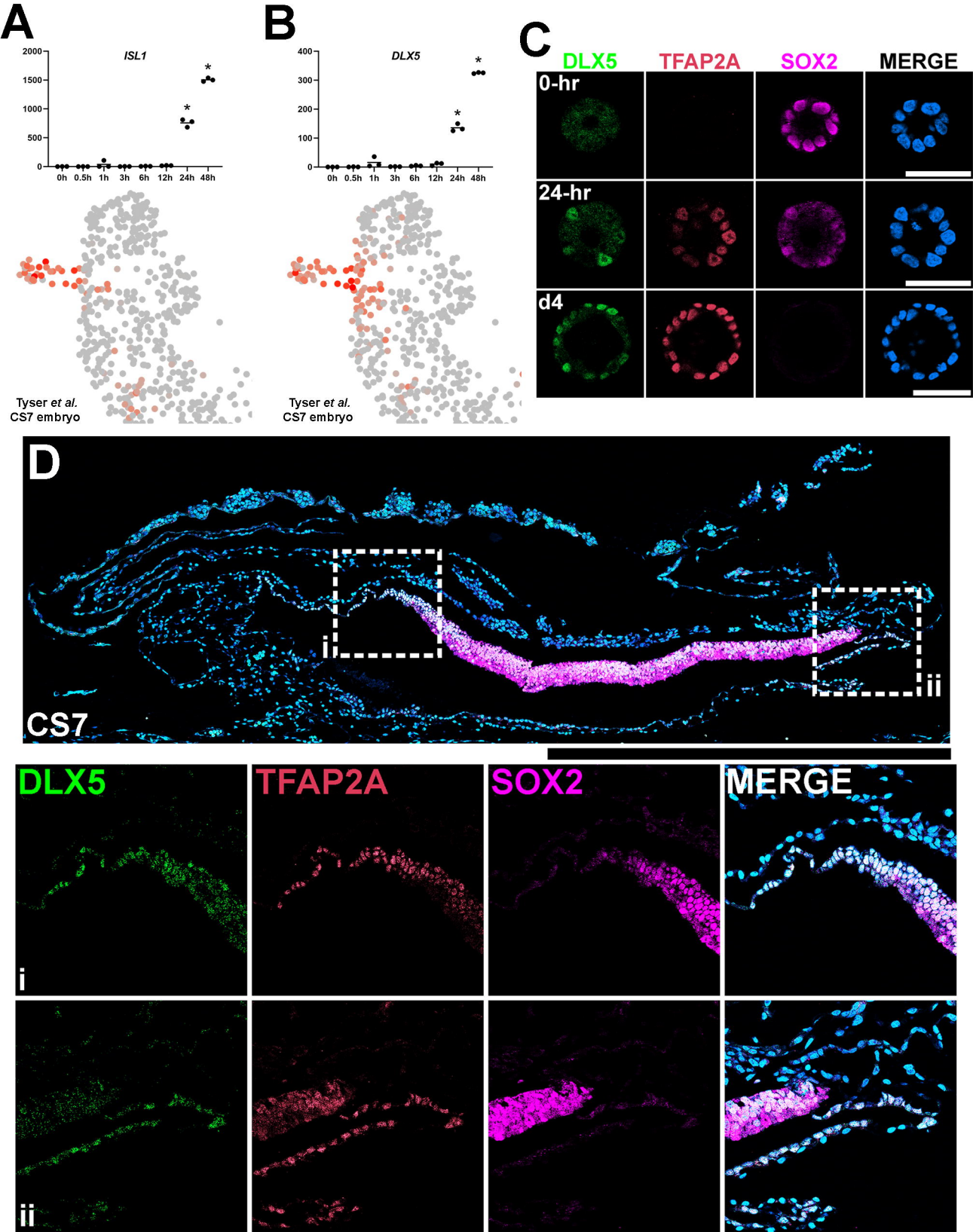
A
ISL1
2000
1500
1000
500
0
0h 0.5h 1h 3h 6h 12h 24h 48h
Tyser et al.
CS7 embryo
B
DLX5
400
300
200
100
0
0h 0.5h 1h 3h 6h 12h 24h 48h
Tyser et al.
CS7 embryo
C
DLX5
TFAP2A
SOX2
MERGE
0-hr
24-hr
d4
D
i
ii
CS7
DLX5
TFAP2A
SOX2
MERGE
i
ii

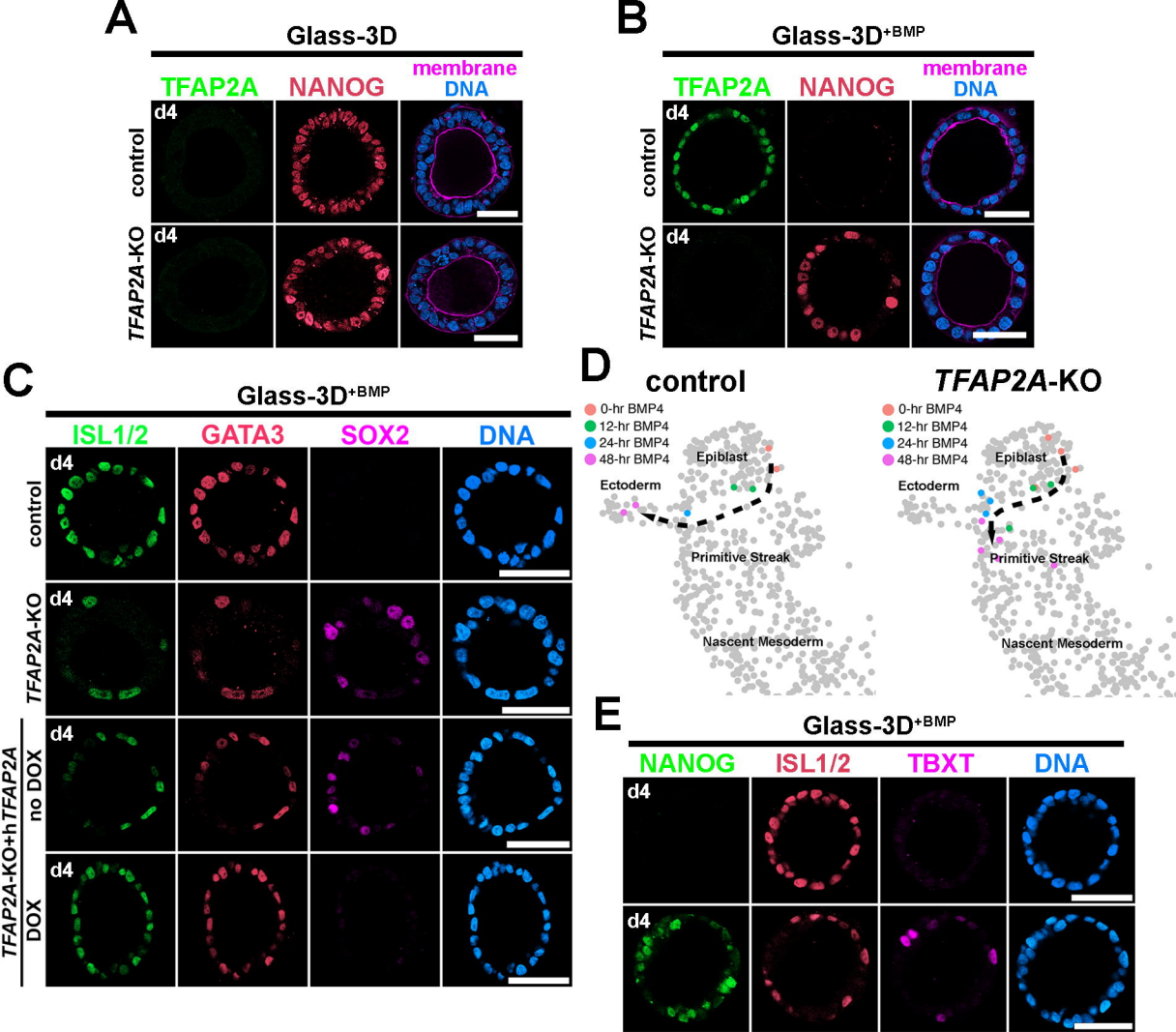
A
Glass-3D
TFAP2A
NANOG
membrane
DNA
control
TFAP2A-KO
d4
B
Glass-3D+BMP
C
ISL1/2
GATA3
SOX2
TFAP2A-KO+hTFAP2A
no DOX
DOX
D
control
TFAP2A-KO
0-hr BMP4
12-hr BMP4
24-hr BMP4
48-hr BMP4
Epiblast
Ectoderm
Primitive Streak
Nascent Mesoderm
E
TBXT